IEEE Access
Multidisciplinary | Rapid Review | Open Access Journal

IEEE POWER & ENERGY SOCIETY SECTION

Received January 3, 2020, accepted February 2, 2020, date of publication February 6, 2020, date of current version February 17, 2020.

Digital Object Identifier 10.1109/ACCESS.2020.2972028

A Robust Frequency-Adaptive Current Control of a Grid-Connected Inverter Based on LMI-LQR Under Polytopic Uncertainties

RIZKA BIMARTA AND KYEONG-HWA KIM, (Member, IEEE)

Research Center for Electrical and Information Technology, Department of Electrical and Information Engineering, Seoul National University of Science and Technology, Seoul 01811, South Korea

Corresponding author: Kyeong-Hwa Kim (k2h1@seoultech.ac.kr)

This work was supported in part by the Basic Science Research Program through the National Research Foundation of Korea (NRF) funded by the Ministry of Education under Grant NRF-2019R1A6A1A03032119, and in part by the Human Resources Development of the Korea Institute of Energy Technology Evaluation and Planning (KETEP) Grant funded by the Korean Government Ministry of Trade, Industry and Energy under Grant 20174030201840.

ABSTRACT This paper presents a frequency-adaptive current control design for a grid-connected inverter (GCI) with an inductive-capacitive-inductive (LCL) filter in the presence of grid disturbance such as the grid frequency variation and grid voltage harmonic distortion as well as polytopic uncertainties in the LCL filter parameters. The grid current control is achieved by augmenting integral and resonant terms into the LCL-filtered inverter system model to constitute integral-resonant full-state feedback control for zero steady-state error and current harmonic attenuation. To realize the full-state feedback control, the information on all the state variables is essential. However, additional sensors for state measurements increase the implementation cost as well as the complexity. To overcome this issue, a full-state discrete-time observer is employed in the stationary reference frame. Furthermore, to maintain the quality of grid currents injected into the grid, a frequency-adaptive current control is introduced. For this aim, the grid frequency is estimated through an adaptive observer rapidly and precisely. Then, the estimated grid frequency is used to adaptively change the frequency information in the augmented resonant controller for the purpose of producing high-quality grid currents even under both distorted grid voltages and grid frequency variation. In addition, to ensure the robustness against LCL filter parameter perturbation, a linear matrix inequality-linear quadratic regulator (LMI-LQR) approach is proposed for polytopic uncertainties in the LCL filter parameters to design full-state feedback control as well as a full-state observer. To verify the effectiveness of the proposed control scheme, the simulation and experimental results are given.

INDEX TERMS Adaptive observer, frequency-adaptive control, grid-connected inverter, linear matrix inequality (LMI), polytopic uncertainties.

I. INTRODUCTION

Over the last several years, renewable energy sources (RESs) such as wind, hydropower, and photovoltaic have been widely developed to replace conventional fossil energy resources. Particularly, RESs are integrated in the form of distributed generation systems (DGSs) [1]. To inject the power from DGSs into the utility grid (UG), a grid-connected inverter (GCI) is commonly adopted as a power interface between RESs and the UG.

The associate editor coordinating the review of this manuscript and approving it for publication was Guangya Yang.

To meet the power quality standard of DGS such as IEEE-519 in the USA or IEC 61000-3-2 in Europe [2], a GCI should produce a high-quality current with low harmonic distortion into the UG. In addition, the injected grid-side currents to the grid should fulfill desired control objectives such as the reference tracking and fast transient response. However, the control design is still challenging due to the grid abnormality such as the harmonic distortion and grid frequency variation, as well as uncertainties in inductive-capacitive-inductive (LCL) filter parameters. Compared with an inductive (L) filter, LCL filters are widely adopted as the link between the GCI and UG due to their better attenuation

capability of the current harmonics [3]. However, LCL filters introduce the resonance behavior which might affect the system stability. In this case, either passive [4] or active [5]–[7] damping method is essential to damp the resonance problem.

To produce high-quality injected grid current under a distorted grid voltage environment, several harmonic attenuation methods have been widely studied. In [8], a grid current active damping control is presented for a single-phase grid-connected inverter. In this scheme, the proportional resonant (PR) and phase-compensated harmonic regulator (HR) are implemented to suppress the harmonics caused by grid voltages distortion. Even though this scheme works well, there exists a trade-off between the control bandwidth and robustness in choosing the PR control gain. Another study proposes an enhanced control structure which integrates the phase-locked loop (PLL) state variables into the controller to design the entire gains based on the optimal control [9]. This structure minimizes the loop interaction between the PLL and controller during the harmonics attenuation process. A feedforward controller based on an implicit zero-sequence discontinuous pulse width modulation (IZDPWM) is applied to an L-filtered grid-connected inverter in [10]. To attenuate current harmonics with the robustness against uncertainties in the grid impedance, an active damping method by using the sliding mode control with a reduced model of a grid-connected inverter is implemented in [11]. Other approaches use a model predictive control [12], the plug-in combination of PR and repetitive control (RC) [13], or multiresonant control [14] to mitigate harmonic currents caused by grid voltage distortion.

A grid frequency fluctuation commonly occurs during the operation of a GCI, which might cause the performance degradation of current control. To resolve such an issue, several frequency-adaptive control schemes have been studied. An enhanced frequency-adaptive current controller based on the RC with a fixed sampling rate is presented in [15] for a single-phase GCI. This approach is realized by approximating the fractional delay with the Lagrange interpolating polynomial for the RC harmonic controller. A similar frequency-adaptive scheme based on the RC with an improved proportional-integral multiresonant (PIMR) scheme is proposed in [16] to consider a wide range of frequency fluctuation from 49.5 Hz to 50.5 Hz for 50 Hz frequency system. In this scheme, the varying fractional delay is realized by a finite impulse response (FIR) filter for adjustment of the controller parameters in order to match its resonant frequency with the grid frequency even when the frequency varies. However, these two methods require a heavier computational task and a higher cost, yielding an overall complexity due to the implementation of the Lagrange interpolating polynomial method [15] or the variation of the sampling rate [16]. In [17], a control method based on a linear parameter varying (LPV) approach is studied for a three-phase inverter to cope with the frequency fluctuation phenomenon. In this method, the control design is accomplished by solving a set of linear matrix inequality (LMI) evaluated on the vertex of a frequency interval to deal with frequency fluctuation in the grid voltage.

As another method to solve the frequency variation issue, a frequency-adaptive control based on the second-order generalized integrator frequency locked loop (SOGI-FLL) is proposed for torque ripple suppression of an induction generator system to consider the stator frequency variation [18]. Despite the effectiveness of the scheme, however, the high bandwidth of the FLL block might cause system instability. A selective harmonic compensator (SHC) by using parallel proportional-integral (PI) and vector-proportional-integral (VPI) controls is also presented in [19] for a three-phase active power filter (APF) to deal with frequency variation and distorted grid condition.

In general, accurate information on the grid frequency is essential for the implementation of a frequency-adaptive current control scheme. For this reason, several frequency estimation approaches have been studied in the literature. In [20], the conventional moving average filter PLL (MAF-PLL) method is adopted to estimate the grid frequency. Even though this method gives a better frequency estimation performance than the conventional PLL, the MAF scheme without using adaptive window length causes a steady-state error of frequency when the frequency varies. Similarly, a cumulative moving average (CMA) filter is presented in [21] to filter out the steady-state frequency error obtained from the PLL. To ensure the performance, the coefficients of the CMA filter should be modified according to the grid frequency variation. For the synchronization of a GCI into the grid, a mixed second- and third-order generalized integrator PLL (MSTOGI-PLL) approach is also proposed in [22]. The performance of this scheme is better than the SOGI-PLL. However, since this method utilizes a high-order system, it has the trade-off between the fast transient response and the ability to attenuate low order harmonics. Instead of direct frequency estimation, another method introduces an adaptive observer which estimates the grid voltage parameters for a single-phase system [23].

Furthermore, when a GCI is linked with LCL filters, a robust control design is necessary to deal with the perturbation issue of filter parameters. In [24], a robust current control scheme of interlink converter for hybrid AC/DC microgrid is implemented to cope with uncertainty in the inductance and resistance of an L filter. In addition, a robust state-feedback control scheme based on the LMI approach is studied in [25], [26]. Even though the robustness of the controller is verified, those methods only consider the parameter uncertainty in the grid-side inductance.

As another approach to tackle the issue related to the uncertainty in the system parameter, the uncertainties in both the inductive-capacitive (LC) filter parameters and the load are taken into account for the controller design of three-phase DC/AC inverter by considering the polytopic model [27]. However, this study is evaluated under only ideal grid voltage condition without consideration of current harmonic attenuation under distorted grid voltages. Another research uses

a robust H_∞ state feedback control to deal with parametric uncertainties in a grid-connected converter [28]. A similar H_∞ control design is proposed in [29] for uninterruptible power supplies to cope with linear load-admittance variation.

In current control design for a GCI with an LCL filter, the computational burden aspect for implementation should be considered, particularly when the grid is in abnormal conditions due to distorted grid, grid frequency variation, and parametric uncertainties. In this case, a control design based on the full-state feedback is well proved to be effective in stabilizing the whole system. However, such a multivariable control design still poses a challenge in selecting appropriate controller gains to achieve a good performance. Related to the gain selection for full-state feedback control, several studies such as the pole placement [30], linear quadratic regulator (LQR) [20], and LMI [25], [26], have been introduced. However, when the number of gains is increased, the pole placement method becomes less attractive due to the time-consuming task. Meanwhile, despite the effectiveness of the LQR approach in obtaining controller gains systematically, the LQR-based control cannot effectively deal with the parametric uncertainty issue. The LQR method is generally designed by minimizing the quadratic cost function with an infinite horizon under the assumption that the parameters in the system model are known [31]. When the system model includes parameter uncertainties, the task of minimizing the cost function for the infinite horizon is difficult [24]. Thus, to overcome this limitation, LMI and LQR approaches are combined, in which the upper bound of the cost function is minimized with the infinite horizon at every sampling period.

In this paper, a robust frequency-adaptive current control for a GCI with an LCL filter is proposed based on the LMI-LQR approach under polytopic uncertainties. The full-state feedback current control is realized by augmenting integral and multiple resonant terms into the system model in order to eliminate the steady-state error and to attenuate the harmonic currents. To avoid control performance degradation caused by the grid frequency fluctuation, the accurate frequency information is essential. Thus, an adaptive observer is adopted to estimate the grid frequency with high accuracy and fast transient response. Moreover, the current control is designed based on an LMI-LQR approach to guarantee the robustness even in the presence of LCL filter parameter perturbation. In addition, to reduce the implementation cost due to the use of full-state feedback control which requires all the system states to be known, a full-state discrete-time observer is employed in the stationary reference frame. In authors' knowledge, most of the existing controllers have not dealt with both the frequency-adaptive issue and the robustness issue against uncertainty in all three LCL parameters at the same time under a distorted grid environment. The main contribution of this study is a robust control design based on the LMI-LQR approach for a GCI under distorted grid condition, frequency variation, and parameter uncertainties with low implementation cost. To validate the effectiveness of the proposed control scheme, the simulation and experimental results are presented.

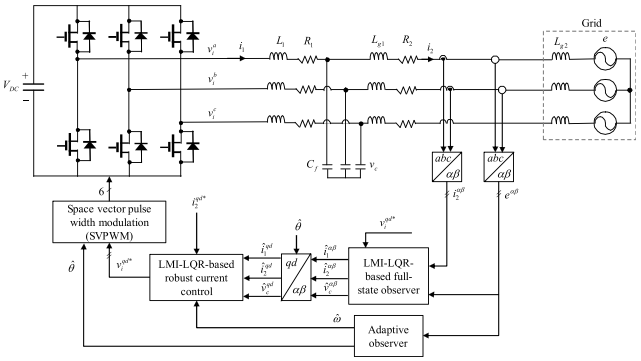

FIGURE 1. Configuration of a GCI and the proposed control scheme.

This paper is organized as follows: Section II explains the system description for a GCI and a model of polytopic uncertainties. Section III presents the proposed robust frequency-adaptive current control scheme. Section IV briefly explains the stability analysis. Section V and VI present the simulation and experimental results to validate the proposed control scheme, respectively. Finally, Section VII concludes the paper.

II. SYSTEM DESCRIPTION

A. SYSTEM MODEL OF GCI IN THE SRF

Fig. 1 shows a configuration of a GCI with an LCL filter and the proposed control scheme which relies on only the measurement of the grid-side currents, grid voltages, and DC link voltage. The proposed scheme is achieved by three main parts which are a frequency-adaptive state feedback current control based on LMI-LQR scheme to produce high-quality grid-side currents even under grid frequency variation, full-state current observer to reduce additional sensors by estimating the system states, and an adaptive observer to estimate the grid frequency, precisely and rapidly. Three-phase GCI is connected into the UG through an LCL filter, in which V_{DC} represents the DC link voltage, R_1 and R_2 are the filter resistances, L_1 and L_{g1} are the filter inductances, C_f is the filter capacitance, and L_{g2} is the grid inductance. The mathematical model of LCL-filter inverter can be obtained by the Kirchhoff's law as follows:

$$\dot{i}_2^{abc} = -R_2 i_2^{abc}/L_2 + v_c^{abc}/L_2 - e^{abc}/L_2 \quad (1)$$

$$\dot{i}_1^{abc} = -R_1 i_1^{abc}/L_1 - v_c^{abc}/L_1 + v_i^{abc}/L_1 \quad (2)$$

$$\dot{v}_c^{abc} = -i_2^{abc}/C_f + i_1^{abc}/C_f \quad (3)$$

where the superscripts "abc" denote the quantities in phase-variable. In addition, i_2 is the grid-side current, i_1 is the inverter-side current, v_c is the capacitor voltage, e is the grid voltage, and v_i is the output voltage of the inverter. Also, the series configuration of L_{g1} and L_{g2} is combined as $L_2 = L_{g1} + L_{g2}$.

The inverter model in the natural frame (1)-(3) can be transformed into the synchronous reference frame (SRF) by

the Park transformation to obtain the state-space model in the SRF as

$$\dot{x}(t) = Ax(t) + Bu(t) + De(t) \tag{4}$$
$$y(t) = Cx(t) \tag{5}$$

where the superscripts "q" and "d" denote the variables in the SRF, $x = \begin{bmatrix} i_2^q & i_2^d & i_1^q & i_1^d & v_c^q & v_c^d \end{bmatrix}^T$ is the system state vector, $u = \begin{bmatrix} v_i^q & v_i^d \end{bmatrix}^T$ is the system input vector, and $e = \begin{bmatrix} e^q & e^d \end{bmatrix}^T$ is the grid voltage vector. The matrices A, B, C, and D are expressed as

$$A = \begin{bmatrix} -R_2/L_2 & -\omega & 0 & 0 & 1/L_2 & 0 \\ \omega & -R/L_2 & 0 & 0 & 0 & 1/L_2 \\ 0 & 0 & -R_1/L_1 & -\omega & -1/L_1 & 0 \\ 0 & 0 & \omega & -R_1/L_1 & 0 & -1/L_1 \\ -1/C_f & 0 & 1/C_f & 0 & 0 & -\omega \\ 0 & -1/C_f & 0 & 1/C_f & \omega & 0 \end{bmatrix}$$
$$B = \begin{bmatrix} 0 & 0 \\ 0 & 0 \\ 1/L_1 & 0 \\ 0 & 1/L_1 \\ 0 & 0 \\ 0 & 0 \end{bmatrix}, \quad D = \begin{bmatrix} -1/L_2 & 0 \\ 0 & -1/L_2 \\ 0 & 0 \\ 0 & 0 \\ 0 & 0 \\ 0 & 0 \end{bmatrix}$$
$$C = \begin{bmatrix} 1 & 0 & 0 & 0 & 0 & 0 \\ 0 & 1 & 0 & 0 & 0 & 0 \end{bmatrix} \tag{6}$$

To discretize the continuous-time model in (4) and (5), the zero-order hold (ZOH) method is applied for digital implementation purpose in which the time delay effect in the control input due to the digital implementation is neglected in this study. With the sampling time T_s, the discrete-time model is obtained as follows:

$$x(k+1) = A_d x(k) + B_d u(k) + D_d e(k) \tag{7}$$
$$y(k) = C_d x(k) \tag{8}$$

where the matrices A_d, B_d, C_d, and D_d can be obtained by

$$A_d = e^{AT_s}, \quad B_d = \left(\int_0^{T_s} e^{AT_s} dt\right) B,$$
$$C_d = C, \quad D_d = \left(\int_0^{T_s} e^{AT_s} dt\right) D.$$

B. MODELING OF POLYTOPIC UNCERTAINTIES

The values of LCL filter parameters in the GCI might vary from the nominal value due to the manufacturing error and temperature effect [24]. In addition, L_2 is also affected by the grid impedance under weak grid [25]. In this paper, it is assumed that the parameters of L_1, L_2, and C_f include uncertainties within a certain range. Namely, LCL filter parameter values in the matrices A and B have the uncertain boundary as follows:

$$L_{1\,\min} \le L_1 \le L_{1\,\max} \tag{9}$$
$$C_{f\,\min} \le C_f \le C_{f\,\max} \tag{10}$$
$$L_{2\,\min} \le L_2 \le L_{2\,\max}. \tag{11}$$

To consider such uncertainty in the system model, the pair of system matrix (A_{di}, B_{di}) with i =1,…,8 denotes eight possible combinations of extreme values of L_1, L_2, and C_f. Furthermore, it is assumed that the system matrix pair (A_{di}, B_{di}) belongs to polytopic uncertain set S as

$$S = \left\{ \sum_{1=1}^{8} \alpha_i (A_{di}, B_{di}) \,\middle|\, \sum_{i=1}^{8} \alpha_i = 1, \alpha_i \ge 0 \right\}. \tag{12}$$

Even though the system parameters can be varied to arbitrary values, they are bounded such that the uncertain ranges of the system parameters are determined as

$$L_{1,nom}/\mu_1 \le L_1 \le \mu_1 L_{1,nom} \tag{13}$$
$$C_{f,nom}/\mu_1 \le C_f \le \mu_1 C_{f,nom} \tag{14}$$
$$L_{2,nom}/\mu_2 \le L_2 \le \mu_2 L_{2,nom} \tag{15}$$

where the subscript "*nom*" denotes the nominal value of LCL filter parameters, and μ_1 and $\mu_2 (\mu_1, \mu_2 > 1)$ are the design parameters [27]. Since L_2 is subject to larger variation than L_1 and C_f due to the effect of grid impedance variation during the operation of GCI, the value of μ_2 is selected as a larger value than that of μ_1.

III. PROPOSED ROBUST FREQUENCY-ADAPTIVE CURRENT CONTROL

In this section, the proposed robust frequency-adaptive current control scheme is designed in the SRF to achieve the control objectives such as zero steady-state error and current harmonic attenuation. An additional objective of the proposed scheme is to guarantee the frequency-adaptive capability under grid frequency variation and the robustness against parameter uncertainties.

A. ADAPTIVE OBSERVER FOR FREQUENCY ESTIMATION

When the grid frequency fluctuates, it might cause the degradation of the current control performance of the GCI since the frequency information in the resonant controller does not match with the real grid frequency [15]. Due to this reason, accurate frequency information is necessary for the online update of the frequency value in the resonant terms. To resolve such an issue, an adaptive observer-based approach is employed to estimate the grid frequency precisely and fast under the distorted grid condition. Fig. 2 shows the detailed block diagram of the adaptive observer for the grid frequency estimation.

In this paper, the adaptive observer is designed in the stationary reference frame with α-axis and β-axis. Since the system models in α-axis and β-axis are decoupled and independent of each other, the observer is designed first in α-axis and the similar approach is applied to β-axis. Assuming that the grid voltages only include the fundamental component without harmonic pollution, the grid voltages are modeled by using a sinusoidal function as follows:

$$\dot{x}_c(t) = M_c x_c(t) \tag{16}$$
$$y_c(t) = N_c x_c(t) \tag{17}$$

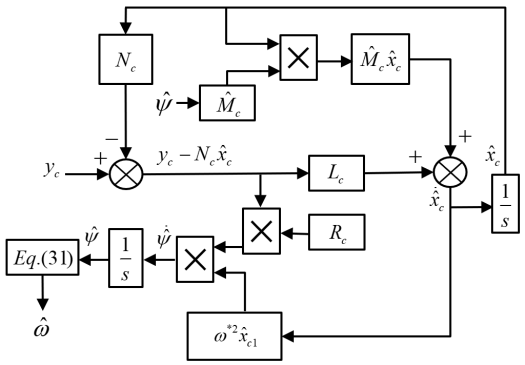

FIGURE 2. Block diagram of the adaptive observer.

where $x_c = [\, x_{c1} \;\; x_{c2} \,]^T$ with being the state vector of the grid voltages expressed as

$$M_c = \begin{bmatrix} 0 & 1 \\ -\omega^{*2}\psi & 0 \end{bmatrix}, \quad N_c = \begin{bmatrix} 1 & 0 \end{bmatrix},$$
$$\psi = \omega^2/\omega^{*2}, \quad \omega^* = 120\pi$$

and ω is the angular frequency of the grid voltage.

To solve the problem related to the estimation of a system with an unknown parameter, an observer for the dynamic system (16) is designed in [23]. In this case, the adaptive observer to estimate the grid voltage parameters is expressed as

$$\dot{\hat{x}}_c(t) = \hat{M}_c\hat{x}_c(t) + L_c[y_c(t) - N_c\hat{x}_c(t)] \tag{18}$$

where $\hat{x}_c$ is the estimated state of x_c

$$\hat{M}_c = \begin{bmatrix} 0 & 1 \\ -\omega^{*2}\hat{\psi} & 0 \end{bmatrix}, \quad L_c = \begin{bmatrix} L_{c1} \\ L_{c2} \end{bmatrix}$$

L_c is the adaptive observer gain and $\hat{\psi}$ is the estimated value of ψ.

It is proved in [23] that an adaptive observer provides superior performance such as zero steady-state estimation error of grid voltage parameters. If the parameter ψ is exactly known in (18), the linear observer (18) would estimate the state x_c asymptotically as long as the observer gain is chosen such that the matrix $(M_c - L_cN_c)$ is Hurwitz. However, under the grid frequency variation, ψ is an unknown parameter. In order to ensure the convergence of the estimated states in (18) to real values, unknown grid frequency should be estimated by an adaptation law. For this purpose, the estimation error of the state and parameter are defined as

$$\tilde{x}_c(t) = x_c(t) - \hat{x}_c(t) \tag{19}$$
$$\tilde{\psi}(t) = \psi(t) - \hat{\psi}(t). \tag{20}$$

Then, the error dynamic of the adaptive observer can be determined from (16)-(18) as

$$\dot{\tilde{x}}_c(t) = (M_c - L_cN_c)\tilde{x}_c(t) - B_c\omega^{*2}\tilde{\psi}\hat{x}_{c1}(t) \tag{21}$$

where $B_c = \begin{bmatrix} 0 & 1 \end{bmatrix}^T$.

Since (21) is non-linear, a Lyapunov stability analysis is performed to prove the stability as described in [23]. By choosing the gain L_c such that $(M_c - L_cN_c)$ is Hurwitz, the system can be strictly positive real. Then, by using the Kalman-Yakubovich-Popov (KYP) lemma [23], [32], there exist $P_c = P_c^T > 0$ and $Q_c = Q_c^T > 0$ such that

$$(M_c - L_cN_c)^T P_c + P_c(M_c - L_cN_c) = -Q_c < 0 \tag{22}$$
$$P_cB_c > N_c^T. \tag{23}$$

To derive the adaptation law, a Lyapunov function can be selected as

$$V(\tilde{x}_c, \tilde{\psi}) = \tilde{x}_c^T P_c\tilde{x}_c + \frac{1}{R_c}\tilde{\psi}^2 \tag{24}$$

where R_c is an adaptive gain. The derivative of the Lyapunov function V can be obtained as

$$\dot{V}(\tilde{x}_c, \tilde{\psi}) = -\tilde{x}_c^T Q_c\tilde{x}_c - 2\tilde{x}_c^T P_cB_c\omega^{*2}\tilde{\psi}\hat{x}_{c1} + \frac{2}{R_c}\tilde{\psi}\dot{\tilde{\psi}} \tag{25}$$

or,

$$\dot{V}(\tilde{x}_c, \tilde{\psi}) = -\tilde{x}_c^T Q_c\tilde{x}_c - 2[y_c(t) - N_c\hat{x}_c(t)]\hat{x}_{c1}\omega^{*2}\tilde{\psi} + \frac{2}{R_c}\tilde{\psi}\dot{\tilde{\psi}}. \tag{26}$$

If the adaptation law is selected as

$$\dot{\hat{\psi}} = -\dot{\tilde{\psi}} = -\omega^{*2}R_c\hat{x}_{c1}[y_c(t) - N_c\hat{x}_c(t)] \tag{27}$$

the derivative function of V can be simplified into

$$\dot{V}(\tilde{x}_c, \tilde{\psi}) = -\tilde{x}_c^T Q_c\tilde{x}_c \leq 0. \tag{28}$$

If (28) holds, the closed-loop system formed by (21) and (27) is globally stable in the sense of Lyapunov. Moreover, in order to prove the global stability by the LaSalle's invariance principle, $\dot{V}(\tilde{x}_c, \tilde{\psi}) = 0$ implies $\tilde{x}_c = 0$. Then, from $\tilde{x}_c = 0$, the error dynamic (21) and the parameter update law (27) yield $\dot{\tilde{\psi}} = 0$. In other words, by the LaSalle's theorem and (28), it is concluded that the adaptive observer (18) and (27) satisfies

$$\lim_{t\to\infty} \tilde{x}_c = \lim_{t\to\infty} (x_c - \hat{x}_c) = 0 \tag{29}$$
$$\lim_{t\to\infty} \tilde{\psi} = \lim_{t\to\infty} (\psi - \hat{\psi}) = 0. \tag{30}$$

Then, by using the relation between unknown parameter ψ and ω, the estimated grid frequency $\hat{\omega}$ can be obtained as

$$\hat{\psi} = \hat{\omega}/\omega^{*2} \rightarrow \hat{\omega} = \hat{\psi} \cdot \omega^{*2}. \tag{31}$$

For a digital implementation of the adaptive observer, the continuous-time adaptive observer in (18) is transformed into the transfer function form as

$$G(s) = \frac{\hat{x}_{c1}(s)}{y_c - N_c\hat{x}_{c1}(s)} = \frac{L_{c1}s + L_{c2}}{s^2 + \omega^{*2}\hat{\psi}}. \tag{32}$$

The transfer function (32) in s-domain is discretized as

$$G(z) = \frac{L_{c1}z^2 - L_{c1}\cos(\omega^{*2}\hat{\psi}T_s)z + L_{c2}}{z^2 - 2\cos(\omega^{*2}\hat{\psi}T_s)z + 1}. \tag{33}$$

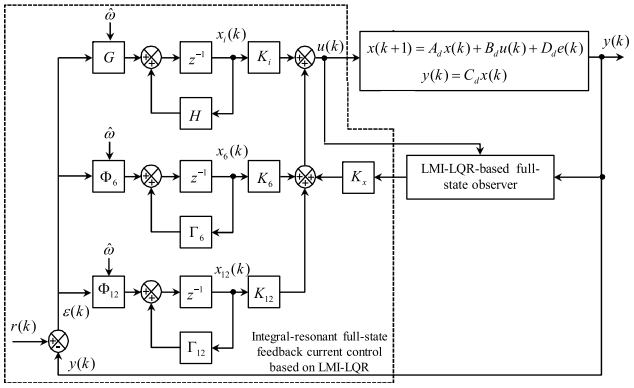

FIGURE 3. Block diagram of the LMI-LQR-based robust current controller.

The transfer function (33) can be expressed in the state-space model as

$$\begin{bmatrix} \hat{x}_{c1}(k+1) \\ \hat{x}_{c2}(k+1) \end{bmatrix} = \begin{bmatrix} 2\cos(\omega^{*2}\hat{\psi}T_s) & 1 \\ -1 & 0 \end{bmatrix} \begin{bmatrix} \hat{x}_{c1}(k) \\ \hat{x}_{c2}(k) \end{bmatrix} + \begin{bmatrix} L_{c1}\cos(\omega^{*2}\hat{\psi}T_s) \\ L_n \end{bmatrix} [y_c(k) - N_c\hat{x}_c(k)] \tag{34}$$

where $L_n = L_{c2} - L_{c1}$.

To consider the harmonic distortion in the grid voltages, the harmonic voltages in the orders 5th, 7th, 11th, and 13th are augmented in the adaptive observer as follows [33]:

$$\hat{x}_e(k+1) = \hat{M}_e\hat{x}_e(k) + L_e[y_e(k) - N_e\hat{x}_e(k)] \tag{35}$$

where $\hat{x}_e = \begin{bmatrix} \hat{x}_{c11} & \hat{x}_{c12} & \hat{x}_{c51} & \hat{x}_{c51} & \cdots & \hat{x}_{c131} & \hat{x}_{c132} \end{bmatrix}^T$

$$\hat{M}_e = \begin{bmatrix} \hat{M}_1 & & & & & & \\ & \hat{M}_5 & & & & & \\ & & \hat{M}_7 & & & & \\ & & & \hat{M}_{11} & & & \\ & & & & \hat{M}_{13} & & \end{bmatrix}, \quad L_e = \begin{bmatrix} L_1 \\ L_5 \\ L_7 \\ L_{11} \\ L_{13} \end{bmatrix}^T$$

$$y_e = \begin{bmatrix} \hat{x}_{c11} & \hat{x}_{c51} & \cdots & \hat{x}_{c131} \end{bmatrix}^T$$

$$N_e = \begin{bmatrix} 1 & 0 & 1 & 0 & \cdots & 1 & 0 \end{bmatrix}$$

$$\hat{M}_i = \begin{bmatrix} 2\cos(i\omega^{*2}\hat{\psi}T_s) & 1 \\ -1 & 0 \end{bmatrix}, \quad L_i = \begin{bmatrix} L_{c1}\cos(i\omega^{*2}\hat{\psi}T_s) \\ L_n \end{bmatrix}$$

for $i = 1, 5, 7, 11, 13$.

By selecting the adaptive observer gain such that the eigenvalues of $(M_e - L_eN_e)$ lie within the unit circle, the estimated states converge to the real values.

B. CURRENT CONTROL BASED ON LMI-LQR APPROACH

The full-state feedback control is implemented to stabilize the whole system. In order to ensure zero steady-state error and the harmonic rejection at 6th and 12th orders, integral and resonant terms are augmented into the system model to construct integral-resonant full-state feedback current controller. Fig. 3 represents the detailed block diagram of a robust current controller based on the LMI-LQR approach. The full-state feedback control and observer gains are obtained systematically by using the LMI-LQR approach in order to overcome the uncertainty issue caused by LCL parameter perturbation.

Integral terms are expressed in the discrete-time state-space as [20]

$$x_i(k+1) = Gx_i(k) + H\varepsilon(k) \tag{36}$$

where $x_i = \begin{bmatrix} x_i^q & x_i^d \end{bmatrix}^T$, $G = I^{2x2}$, $H = T_s \times I^{2x2}$ $\varepsilon = \begin{bmatrix} \varepsilon^q & \varepsilon^d \end{bmatrix}^T = r - C_dx$ is the grid-side current error, and $r = \begin{bmatrix} i_2^{q*} & i_2^{d*} \end{bmatrix}^T$ is the reference.

In addition to the robustness against LCL parameter uncertainty, to ensure the frequency-adaptive capability of the proposed current control under grid frequency deviation and grid harmonic distortion, resonant terms are augmented, in which the frequency is updated with online by using the frequency information estimated from the adaptive observer.

To implement the resonant controller in the discrete-time, the transfer function of resonant terms in the z-domain is employed to compensate for the harmonics in the 6th and 12th orders [34]. It is well known that this method does not yield the performance degradation caused by frequency deviation at high resonant frequency during the discretization process. A discrete-time transfer function of the resonant terms is expressed as [34]

$$R_h(z) = \frac{z^2 - \cos(\omega_h T_s)z}{z^2 - 2\cos(\omega_h T_s)z + 1} \tag{37}$$

where ω_h is the resonant angular frequency. The transfer function in (37) can be expressed in the state-space as [35]

$$r_h(k+1) = M_h r_h(k) + N_h\varepsilon(k) \tag{38}$$

where $M_h = \begin{bmatrix} 2\cos(h\omega_h T_s) & 1 \\ -1 & 0 \end{bmatrix}$, $N_h = \begin{bmatrix} \cos(h\omega_h T_s \\ -1 \end{bmatrix}$.

Based on (38), the resonant terms for q-axis and d-axis in h-th harmonic order are modeled in the state-space as

$$x_h(k+1) = \Phi_h x_h(k) + \Gamma_h\varepsilon(k) \tag{39}$$

where

$$x_h = \begin{bmatrix} x_{1h}^q & x_{2h}^q & x_{1h}^d & x_{2h}^d \end{bmatrix}^T$$

$$\Phi_h = \begin{bmatrix} M_h & 0 \\ 0 & M_h \end{bmatrix}, \Gamma_h = \begin{bmatrix} N_h & 0 \\ 0 & N_h \end{bmatrix} \text{ for } h = 6, 12.$$

Each of the resonant terms for harmonic order h introduces four additional states into the inverter system model. Then, the integral control terms in (36) and resonant control terms in (39) are combined into the system state model by including polytopic uncertainty as follows:

$$x_g(k+1) = A_{gi}x_g(k) + B_{gi}u(k) + D_ge(k) + B_{rg}r(k) \tag{40}$$

$$y(k) = C_gx_g(k) \tag{41}$$

where $x_g = \begin{bmatrix} x & x_i & x_6 & x_{12} \end{bmatrix}^T$ with the length of 16

$$A_{gi} = \begin{bmatrix} A_{di} & 0 & 0 & 0 \\ -HC_d & G & 0 & 0 \\ -\Gamma_6 C_d & 0 & \Phi_6 & 0 \\ -\Gamma_{12} C_d & 0 & 0 & \Phi_{12} \end{bmatrix}, \quad B_{gi} = \begin{bmatrix} B_{di} \\ 0 \\ 0 \\ 0 \end{bmatrix},$$

$$D_g = \begin{bmatrix} D_d \\ 0 \\ 0 \\ 0 \end{bmatrix}$$

$$B_{rg} = \begin{bmatrix} 0^T & H^T & \Gamma_6^T & \Gamma_{12}^T \end{bmatrix}^T, \quad C_g = \begin{bmatrix} C_d & 0 & 0 & 0 \end{bmatrix}$$

for $i = 1, \ldots 8$.

To design the control input $u(k)$ such that the system is stable, the state-feedback control is used as $u(k) = Kx_g(k)$ with $K = \begin{bmatrix} K_x & K_i & K_6 & K_{12} \end{bmatrix}$. In order to ensure the control performance and system stability, the feedback gain K is evaluated systematically by minimizing the quadratic cost function as follows:

$$\min_{u(k)} J_\infty = \sum_{k=0}^{\infty} \left\{ x_g(k)^T Q x_g(k) + u(k)^T R u(k) \right\}. \quad (42)$$

By considering a quadratic Lyapunov equation as

$$V(k) = x_g(k)^T P x_g(k) \quad (43)$$

where $P = Y^{-1}$ is a positive definite matrix, the system model in (40) with the full-state feedback control $u(k)$ is stable if and only if

$$V(k+1) - V(k) \leq -\left\{ x_g(k)^T Q x_g(k) + u(k)^T R u(k) \right\} \quad (44)$$

or,

$$(A_{gi} + B_{gi}K)^T P (A_{gi} + B_{gi}K) - P \leq -Q - K^T R K. \quad (45)$$

Multiplying the matrix Y on the left- and right-hand sides of (45) yields

$$Y - Y^T Q Y - L^T R L - (A_{gi}Y + B_{gi}L)^T Y^{-1} (A_{gi}Y + B_{gi}L) \geq 0 \quad (46)$$

where $L = KY$. Applying Schur complement to (46) yields [36]

$$\begin{bmatrix} Y & L^T & (A_{gi}Y + B_{gi}L)^T & Y \\ L & R^{-1} & 0 & 0 \\ (A_{gi}Y + B_{gi}L) & 0 & Y & 0 \\ Y & 0 & 0 & Q^{-1} \end{bmatrix} \geq 0, \quad (47)$$

for $i = 1, \ldots, 8$.

In general, when the system model does not include uncertainties, the gain is calculated in LQR control by minimizing the cost function over the whole horizon. Thus, LQR is normally called an infinite horizon control problem of (42) [24]. However, the uncertainty in the system model causes difficulty in solving the minimization problem. To overcome this limitation, the feedback gain is computed by minimizing the upper bound J_∞ at every sampling time. Furthermore, in order to ensure robust performance, the sum of Lyapunov difference is evaluated as [24]

$$\sum_{k=0}^{\infty} \{V(k+1) - V(k)\} \leq \sum_{k=0}^{\infty} -\left\{ x_g(k)^T Q x_g(k) + u(k)^T R u(k) \right\}. \quad (48)$$

This is equivalent to $V(\infty) - V(0) \leq -J_\infty$, in which J_∞ denotes the optimal cost function for the infinite horizon. If the control stabilizes the system, it holds $V(\infty) = 0$. Thus, it yields $J_\infty \leq V(0)$, which indicates that $V(0)$ is the upper bound of the LQR cost function. In addition, if α denotes the upper bound of $V(0)$, the following equation holds

$$J_\infty \leq V(0) = x_g(0)^T P x_g(0) \leq \alpha \quad (49)$$

or,

$$\begin{bmatrix} \alpha & x_g(0)^T \\ x_g(0) & P^{-1} \end{bmatrix} \geq 0. \quad (50)$$

Therefore, an optimal gain K of the state-feedback control can be determined by solving the following optimization problem as

$$\min_{Y,L,\alpha} \alpha \quad subject\ to \begin{bmatrix} E & 0 & 0 \\ 0 & \alpha & x_g(0)^T \\ 0 & x_g(0) & P^{-1} \end{bmatrix} \geq 0 \quad (51)$$

where E denotes the matrix in (47). It should be noted that by solving (51), the condition of (46) holds. Thus, the overall stability is guaranteed as long as uncertainties in L_1, L_2, and C_f belong to the ranges in (13)-(15). Then, the state feedback gain is obtained as $K = LY^{-1}$ to ensure that the closed-loop system (40) is robustly stable. In this paper, the weighting matrices Q and R are selected as

$$Q = diag[0.98 \times I^{6\times6}, 10^8 \times I^{2\times2}, 0.2 \times I^{4\times4}, 0.4 \times I^{4\times4}]$$

$$R = I^{2\times2}.$$

C. FULL-STATE CURRENT OBSERVER BASED ON LMI-LQR APPROACH

To implement a full-state feedback control, the information on the whole system states is necessary. Since additional sensors to measure the system states increase the implementation cost, a full-state current observer is employed to estimate the system states without additional sensors. The system model (4) in the SRF includes the grid frequency information. To obtain the discretized model of (4) under frequency variation, only the online discretization process is possible because the frequency is considered as a time-varying parameter. In general, the ZOH method is preferred to obtain a discretized system model [37]. However, calculating a discretized model by using the ZOH method by online with the time-varying parameter is a complex task. To avoid such a drawback, the full-state observer is implemented in the stationary reference frame since the system model does not include the frequency information in the stationary

reference frame. Then, the online discretization process based on the ZOH method can be avoided. Instead, the conventional offline discretization method can be simply used [20].

The system model of the GCI in the state-space is expressed in the stationary reference frame as

$$\dot{x}_s(t) = A_s x_s(t) + B u_s(t) + D e_s(t) \tag{52}$$
$$y_s(t) = C x_s(t) \tag{53}$$

where superscripts "α" and "β" denote the variables in the stationary reference frame, $x_s = \begin{bmatrix} i_2^\alpha & i_2^\beta & i_1^\alpha & i_1^\beta & v_c^\alpha & v_c^\beta \end{bmatrix}^T$ is the system state vector, $u_s = \begin{bmatrix} v_i^\alpha & v_i^\beta \end{bmatrix}^T$ is the system input vector, and $e_s = \begin{bmatrix} e^\alpha & e^\beta \end{bmatrix}^T$ is the grid voltage vector. The matrices B, C, and D are defined as the same in (6) while the matrix A_s is expressed as

$$A_s = \begin{bmatrix} -R_2/L_2 & 0 & 0 & 0 & 1/L_2 & 0 \\ 0 & -R/L_2 & 0 & 0 & 0 & 1/L_2 \\ 0 & 0 & -R_1/L_1 & 0 & -1/L_1 & 0 \\ 0 & 0 & 0 & -R_1/L_1 & 0 & -1/L_1 \\ -1/C_f & 0 & 1/C_f & 0 & 0 & 0 \\ 0 & -1/C_f & 0 & 1/C_f & 0 & 0 \end{bmatrix}$$

The system model in (52) and (53) are then discretized using the ZOH method as

$$x_s(k+1) = A_{sd} x_s(k) + B_{sd} u_s(k) + D_{sd} e_s(k) \tag{54}$$
$$y_s(k) = C_{sd} x_s(k). \tag{55}$$

Similar to (40), by considering the uncertainties of LCL parameters, (54) and (55) can be expressed including polytopic uncertainty as

$$x_s(k+1) = A_{sdi} x_s(k) + B_{sdi} u_s(k) + D_{sd} e_s(k) \tag{56}$$
$$y_s(k) = C_{sd} x_s(k) \tag{57}$$

for $i = 1, \ldots, 8$.

In this paper, to estimate all the system states, a discrete-time full-state current-type observer is employed due to its advantages as compared to the predictive-type observer. From the discrete-time system model in (56), the current-type observer can be constructed as

$$\bar{x}_s(k+1) = A_{sdi} \hat{x}_s(k) + B_{sdi} u_s(k) + D_{sd} e_s(k) \tag{58}$$
$$\hat{x}_s(k+1) = \bar{x}_s(k+1) + K_o[y_s(k+1) - C_{sd} \bar{x}_s(k+1)] \tag{59}$$

where the symbol "^" denotes the estimated quantities, K_o is the observer gain matrix. If the estimation error is defined as

$$\tilde{x}_s(k) = x_s(k) - \hat{x}_s(k) \tag{60}$$

the error dynamic can be determined from (56) and (59) as

$$\tilde{x}_s(k+1) = (A_{sdi} - K_o C_{sd} A_{sdi}) \tilde{x}_s(k). \tag{61}$$

By applying similar procedures as in (42) through (45), the inequality for the state estimator is expressed as

$$P_o - Q_o - K_o^T R_o K_o - (A_{sdi} - K_o C_{sd} A_{sdi})^T P_o (A_{sdi} - K_o C_{sd} A_{sdi}) \geq 0 \tag{62}$$

where $P_o = Y_o^{-1}$ is a positive definite matrix. Furthermore, multiplying the matrix Y_o on the left- and right-hand sides of (62) yields

$$Y_o - Y_o^T Q_o Y_o - L_o^T R_o L_o - (A_{sdi} Y_o - L_o C_{sd} A_{sdi})^T Y_o^{-1} (A_{sdi} Y_o - L_o C_{sd} A_{sdi}) \geq 0 \tag{63}$$

where $L_o = K_o Y_o$. Then, the Schur complement can be similarly applied to the inequality (63) as [36]

$$\begin{bmatrix} Y_o & L_o^T & (A_{sdi} Y_o - L_o C_{sd} A_{sdi})^T & Y_o \\ L_o & R_o^{-1} & 0 & 0 \\ (A_{sdi} Y_o - L_o C_{sd} A_{sdi}) & 0 & Y_o & 0 \\ Y_o & 0 & 0 & Q_o^{-1} \end{bmatrix} \geq 0, \quad \text{for } i = 1, \ldots, 8. \tag{64}$$

Similar to the previous approach which considers the sum of Lyapunov difference in (48) in order to obtain robust performance capability, the upper bound for the observer system can be also determined as

$$J_\infty \leq V_o(0) = x_s(0)^T P_o x_s(0) \leq \alpha_o \tag{65}$$

or,

$$\begin{bmatrix} \alpha_o & x_s(0)^T \\ x_s(0) & P_o^{-1} \end{bmatrix} \geq 0. \tag{66}$$

If the matrices $Y_o > 0$ and $L_o > 0$ exist, an optimal gain K_o of the full-state observer can be determined by solving the following optimization problem as

$$\min_{Y_o, L_o, \alpha_o} \alpha_o \quad \textit{subject to} \quad \begin{bmatrix} E_o & 0 & 0 \\ 0 & \alpha_o & x_s(0)^T \\ 0 & x_s(0) & P_o^{-1} \end{bmatrix} \geq 0 \tag{67}$$

where E_o denotes the matrix in (64). It should be also noted that by solving (67), the condition of (63) holds. Thus, the overall stability is guaranteed as long as the uncertainties in L_1, L_2, and C_f belong to the ranges in (13)-(15). Then, the observer gain is obtained as $K_o = L_o Y_o^{-1}$ to ensure that the closed-loop system (59) is robustly stable.

IV. STABILITY ANALYSIS

The location of the eigenvalues of the closed-loop system in the z-plane is influenced by the variation of the grid impedance or LCL filter parameters. To ensure the control robustness, all the eigenvalues should stay in the stable regions even under the parameter variations. To cope with parametric uncertainties, the eight possible combinations of extreme values of the LCL filter parameters given in (9)-(11) are applied. Then, by solving the optimization for eight LMI problems which include these eight combinations, the robust state feedback gains are obtained. To prove that the entire system is stable under the parameter uncertainties within the extreme values of the LCL filter parameters, the eigenvalues of the closed-loop system for the eight possible combinations of extreme values are investigated.

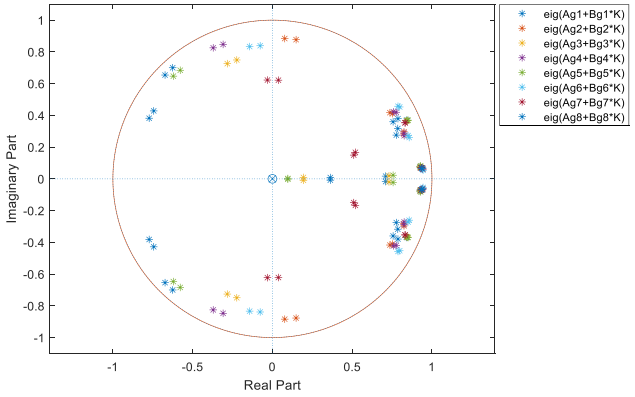

FIGURE 4. Eigenvalues of the closed-loop system in the proposed control scheme for eight combinations of LCL filter parameter values.

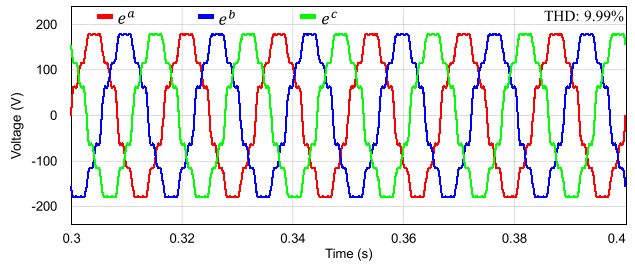

FIGURE 5. Three-phase distorted grid voltages.

TABLE 1. System parameters of a grid-connected inverter.

Parameter	Symbol	Value	Units
DC-link voltage	V_{DC}	420	V
Resistance (load bank)	R	24	Ω
Filter resistance	R_1, R_2	0.5	Ω
Nominal filter capacitance	C_f	4.5	μF
Nominal inverter-side filter inductance	L_1	1.7	mH
Nominal grid-side filter inductance	L_{g1}	1.7	mH
Nominal grid inductance	L_{g2}	0	mH
Grid voltage (line-to line rms)	e	220	V
Nominal grid frequency	f_n	60	Hz

Fig. 4 shows the eigenvalues of the closed-loop system in the proposed control scheme for eight combinations of LCL filter parameter values. As can be seen from this figure, all the eigenvalues stay inside the boundary of the unit circle even under the uncertainties in LCL filter parameters. Furthermore, all the eigenvalues remain inside the unit circle despite the variation of LCL filter parameter values, which clearly indicates the robustness of the proposed control scheme against parameter uncertainty.

V. SIMULATION RESULTS

This section presents the simulation results by using the PSIM software to validate the feasibility of the proposed robust frequency-adaptive current control scheme for a GCI with an LCL filter. The overall configuration of the proposed control scheme is depicted in Fig. 1 through Fig. 3. The system parameters of a GCI are listed in Table 1.

Fig. 5 shows three-phase distorted grid voltages with the harmonic contamination in the orders of 5^{th}, 7^{th}, 11^{th}, and 13^{th} with a 5% magnitude of the nominal grid voltage. These distorted grid voltages are combined with grid frequency variation to demonstrate the performance of the proposed current control scheme in regards of the quality of the injected grid-side currents.

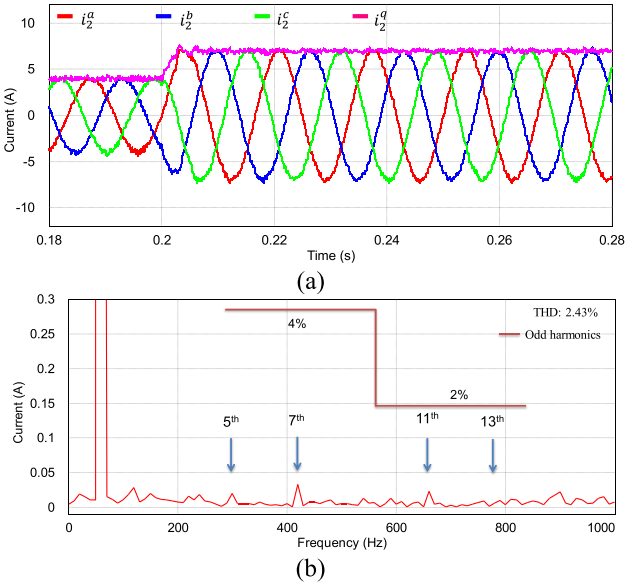

FIGURE 6. Simulation results for the proposed control scheme. (a) Waveforms of grid-side three-phase currents and q-axis current. (b) FFT result for a-phase grid-side current.

Fig. 6(a) represents the simulation results for the proposed control scheme under distorted grid condition as in Fig. 5 with a step change in the current reference at 0.2 s from 4 A to 7 A. Waveforms of grid-side three-phase currents and q-axis current prove that the proposed current controller can track the reference with satisfactory transient and steady-state performance. Fig. 6(b) shows the FFT result for steady-state a-phase current. It is clearly shown that all the harmonic components existing in distorted grid voltages can be well damped by the proposed control scheme, generating the total harmonic distortion (THD) value of 2.43%. This value meets the criteria specified by the grid interconnection regulation IEEE Std. 1547 for inverter-injected current [38].

Fig. 7 shows the comparative simulation results for frequency estimation performance between the adaptive observer scheme and the conventional MAF-PLL method. Fig. 7(a) shows the performance comparison when the grid frequency varies from 60 Hz to 58 Hz at 0.5 s, and then, from 58 Hz to 63 Hz at 0.6 s under distorted grid. It is observed that the dynamic response of the frequency estimation scheme by the adaptive observer is faster to reach the steady-state condition. Moreover, after the grid frequency changes, the MAF-PLL scheme shows a larger frequency ripple without the adjustment of window length in the MAF [39]. To further demonstrate the frequency estimation performance, distorted grid, grid frequency variation, and grid phase jump are considered at the same time as depicted in Fig. 7(b), in which the phase jump of $-30°$ at 0.5 s and $30°$ at 0.6 s are applied

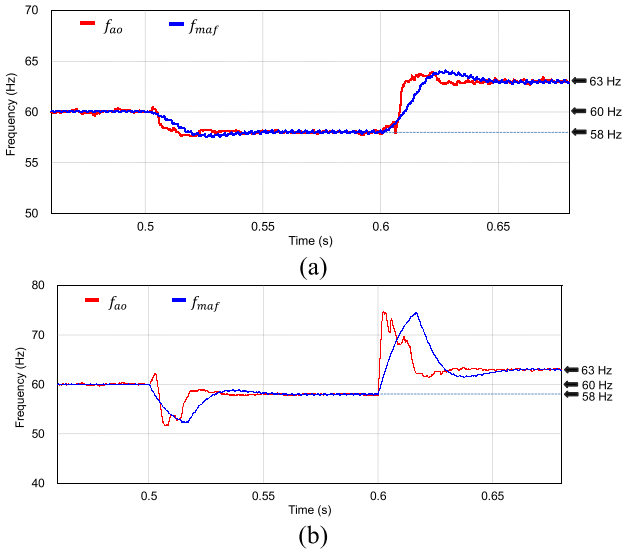

FIGURE 7. Comparative simulation results for frequency estimation between the adaptive observer and MAF-PLL. (a) Under frequency variation from 60 Hz to 58 Hz at 0.5 s and from 58 Hz to 63 Hz at 0.6 s. (b) Under frequency variation from 60 Hz to 58 Hz and phase jump of $-30°$ at 0.5 s, and frequency variation from 58 Hz to 63 Hz and phase jump of 30° at 0.6 s.

to the grid in addition to both distorted grid and frequency variation. It can be clearly seen that the transient response of the adaptive observer is much faster than the MAF-PLL to reach the steady-state. This estimated frequency is employed to adaptively adjust the frequency information in resonant control terms to achieve a frequency-adaptive capability of the current control.

Fig. 8 shows the simulation results for the proposed control scheme under frequency variation from 60 Hz to 58 Hz at 0.5 s, and from 58 Hz to 63 Hz at 0.6 s. Fig. 8(a) represents the grid-side current response in the SRF. As the grid frequency changes, transient current oscillation is observed. However, the currents can be stabilized immediately and reach steady-state values again. The response of three-phase grid-side currents under frequency variation is depicted in Fig. 8(b). When the grid frequency instantaneously changes, small distortion is shown in current waveforms. However, this current distortion due to frequency change is completely compensated within only half a cycle. In Fig. 8(b), the THD values of phase currents which are measured by using steady-state phase currents are presented as 2.43% at 60 Hz, 2.46% at 58 Hz, and 2.51% at 63 Hz, respectively. These values fulfill the harmonic restriction specified by the grid interconnection criteria. Furthermore, to clearly show the transient response of grid-side currents, enlarged waveforms of Fig. 8(b) are presented in Fig. 8(c) for the frequency change from 60 Hz to 58 Hz, and in Fig. 8(d) for the frequency change from 58 Hz to 63 Hz, respectively. Both figures show a fast transient and a good harmonic attenuation capability of the proposed control scheme even under severe harmonic distortion and frequency variation in grid voltages.

To further evaluate the effectiveness of the proposed control scheme, the phase jump condition is also applied to the

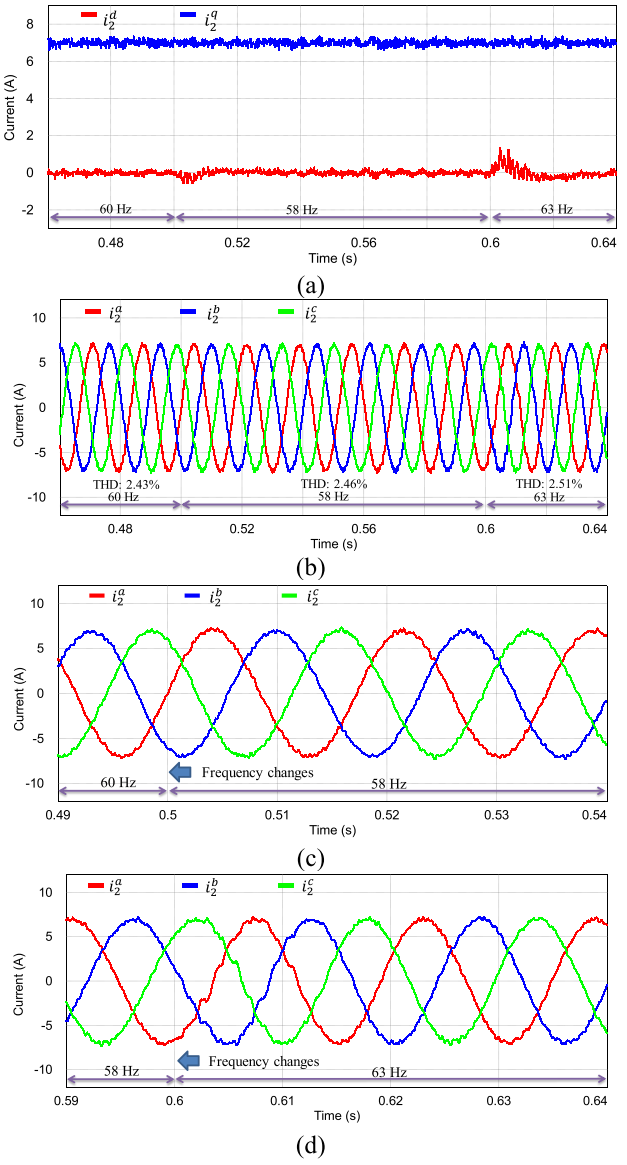

FIGURE 8. Simulation results for the proposed control scheme under frequency change from 60 Hz to 58 Hz at 0.5 s, and from 58 Hz to 63 Hz at 0.6 s. (a) Grid-side currents in the SRF. (b) Three-phase grid-side current waveforms. (c) Enlarged waveforms of three-phase grid-side currents when the frequency changes from 60 Hz to 58 Hz at 0.5 s. (c) Enlarged waveforms of three-phase grid-side currents when the frequency changes from 58 Hz to 63 Hz at 0.6 s.

grid in addition to both distorted grid and frequency variation. Fig. 9(a) represents the simulation results for the proposed control scheme when the grid voltages have frequency variation, phase jump, and harmonic distortion at the same time. In this simulation, the grid voltage experiences both the frequency change from 60 Hz to 58 Hz and the phase jump of $-30°$ at 0.5 s, and both the frequency change from 58 Hz to 63 Hz and the phase jump of 30° at 0.6 s. Fig. 9(b) and Fig. 9(c) show the enlarged waveforms at each transient condition. Even though small overshoot currents are observed due to a sudden phase jump of the grid voltage, peak currents are within an acceptable boundary and phase-currents are

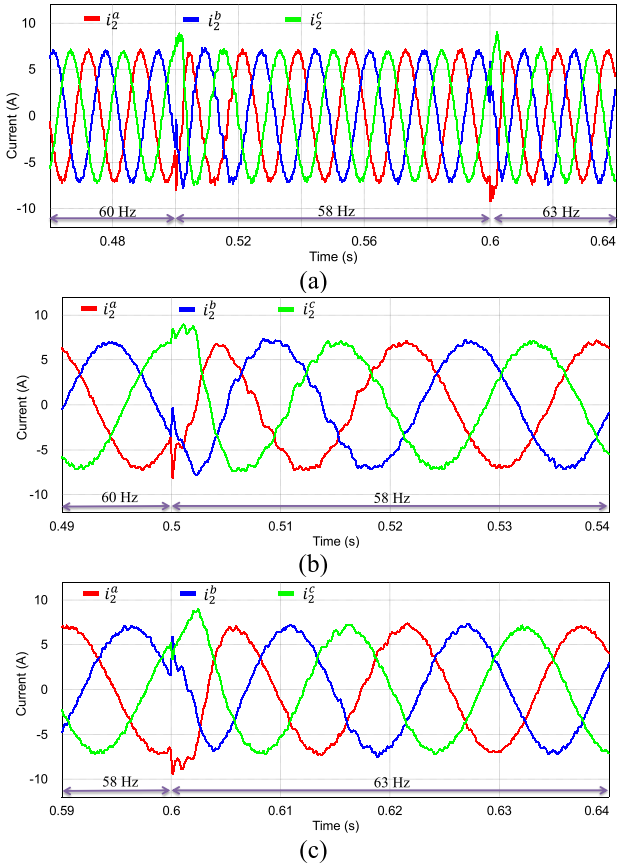

FIGURE 9. Simulation results for the proposed control scheme under frequency change and phase jump. (a) Three-phase grid-side currents. (b) Enlarged waveforms of three-phase grid-side currents under frequency change from 60 Hz to 58 Hz and phase jump of −30° at 0.5 s. (c) Enlarged waveforms of three-phase grid-side currents under frequency change from 58 Hz to 63 Hz and phase jump of 30° at 0.6 s.

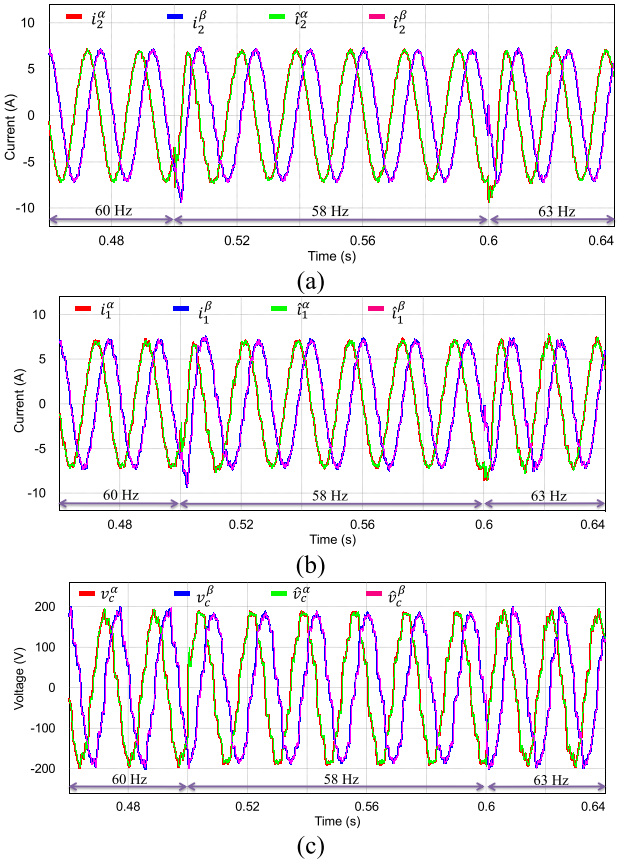

FIGURE 10. Simulation results for the observer estimation performance in the stationary reference frame under frequency variation and phase jump (60 Hz → 58 Hz, −30° at 0.5 s and 58 Hz → 63 Hz, 30° at 0.6 s with the nominal LCL filter parameters. (a) Grid-side currents and estimated states. (b) Inverter-side currents and estimated states. (c) Capacitor voltages and estimated states.

quickly recovered to sinusoidal values, which proves that the proposed scheme can stabilize the entire system in the presence of such severe grid uncertainty.

To evaluate the observer estimation performance, Fig. 10 shows the simulation results for the discrete-time current observer in the stationary reference frame when the grid voltage has frequency variation, phase jump, and harmonic distortion at the same time. In this test, the grid condition is the same as Fig. 9. Fig. 10(a), Fig. 10(b), and Fig. 10(c) show the measured and estimated states for the grid-side currents, inverter-side currents, and capacitor voltages, respectively. As is shown noticeably, the estimated states well converge to real values even when the frequency variation and phase jump are applied to the grid simultaneously. As a result, a fast and robust estimating performance of observers can be obtained through the gain selection based on the LMI-LQR approach.

To test the robustness of the proposed control scheme under LCL filter parameter variations, Fig. 11 shows the simulation results for three-phase grid-side currents with the proposed control scheme when the LCL filter parameter values are suddenly changed from the nominal values. In (13)-(15), the design parameters for uncertainty ranges are chosen as $\mu_1 = 1.4$ and $\mu_2 = 2.0$. The value of μ_2 is chosen as a higher value to consider the grid impedance variation effect during the operation of a GCI. As is clearly seen in Fig. 11(a) and Fig. 11(b), the proposed control scheme based on the LMI-LQR approach yields a robust current control performance even when LCL filters are suddenly changed. Three-phase grid-side currents are recovered to sinusoidal values within 10 ms, which demonstrates the robustness of the proposed control scheme against the parameter perturbation.

Furthermore, to evaluate the robustness against LCL filter parameter perturbation, comparative simulations with the existing frequency-adaptive control schemes are performed with a larger variation of LCL filter parameters. Fig. 12 shows the comparative simulation results for three-phase grid-side currents for the studies in [20] and [33], and the proposed control scheme when LCL filter parameters are suddenly varied from the nominal values to $L_1 = 0.5mH$, $C_f = 1.5\mu F$, and $L_2 = 0.4mH$ at 0.5 s. In the proposed scheme, the controller is designed by increasing the design parameters $\mu_1 = 3.0$ and $\mu_2 = 4.0$ to obtain new set of control gains. Fig. 12(a) and Fig. 12(b) show the current responses with the method in [20], and in [33], respectively. As can be observed

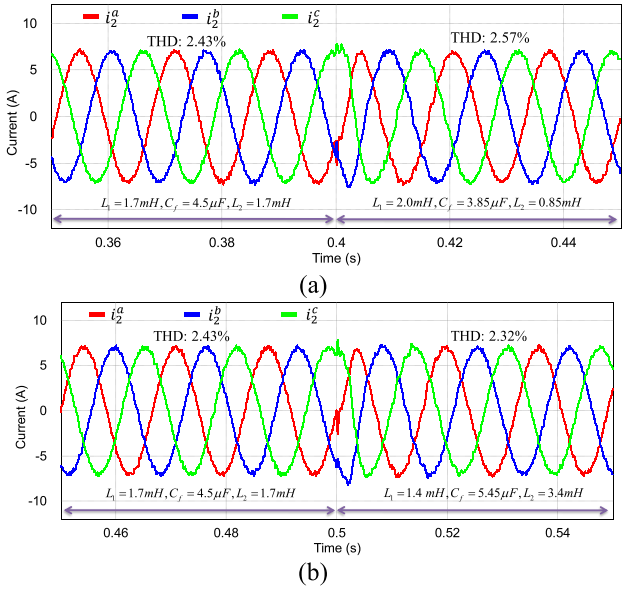

FIGURE 11. Simulation results for three-phase grid-side currents with the proposed control scheme under sudden LCL filter parameter variations. (a) LCL parameters are changed to $L_1 = 2.0mH$, $C_f = 3.85\mu F$, $L_2 = 0.85mH$ at 0.4 s. (b) LCL parameters are changed to $L_1 = 1.4mH$, $C_f = 5.45\mu F$, $L_2 = 3.4mH$ at 0.5 s.

from these figures, when the LCL filter parameters vary in a large range, the controller cannot stabilize the system. On the other hand, as depicted in Fig. 12(c), the proposed scheme is still able to stabilize the system even under such a larger LCL filter parameter perturbation due to robust control design by incorporating the model of polytopic uncertainties in the system model. The proposed control scheme in Fig. 12(c) yields a mere increase in THD value as compared to the result in Fig. 11 caused by the LCL filter change. These comparative results effectively prove that the proposed scheme possesses the robustness against LCL parameter variation.

In order to verify the frequency-adaptive capability of the proposed scheme with new design parameter values, the simulation result under frequency variation is presented in Fig. 13 when the grid frequency decreases from 60 Hz to 58 Hz at 0.5 s, and increases from 58 Hz to 63 Hz at 0.6 s. The transient response of phase currents is slower as compared to the case which has a smaller uncertainty range in Fig. 8(b). However, the proposed controller can stabilize the inverter system, reaching the steady-state in less than 2 cycles. The THD values for steady-state current in each frequency are 3.02% at 60 Hz, 3.11% at 58 Hz, and 3.18% at 63 Hz, which satisfy the grid harmonic criteria.

In a three-phase GCI, the PLL is commonly used for the synchronization with grid, and the PLL dynamics are the key factors for a stable operation of inverters. However, in the weak grid condition, the dynamics of the PLL are affected by high grid impedance because the coupling between PLL and grid impedance causes the harmonic resonance or even system instability as studied in [40], [41]. The dynamic of

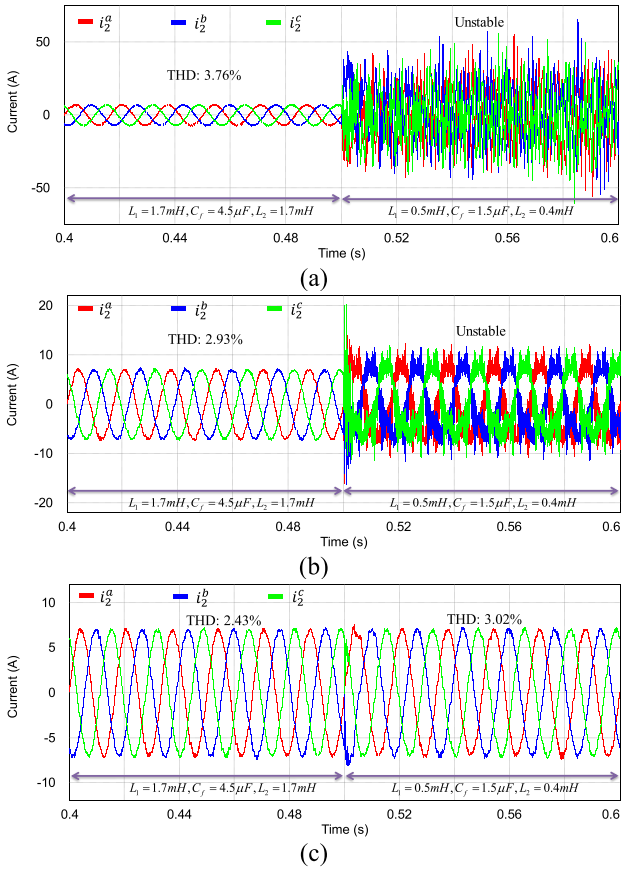

FIGURE 12. Comparative simulation results for three-phase grid-side currents under sudden LCL filter parameter variations from the nominal values. (a) With [20]. (b) With [33]. (c) With the proposed control scheme.

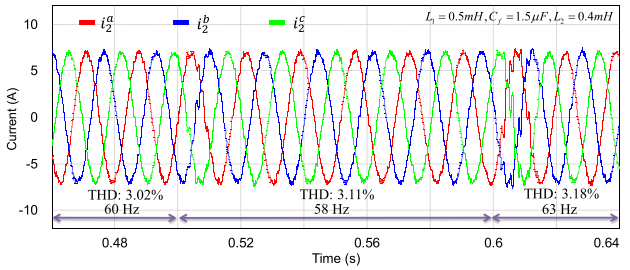

FIGURE 13. Simulation result for the proposed control scheme with $\mu_1 = 3.0$ and $\mu_2 = 4.0$ under frequency variation.

LCL filters or the value of L_2 may also be affected by the grid impedance variation [42]. In order to investigate the effect of L_{g1} and L_{g2} on phase angle detection, Fig. 14 shows the simulation results for phase angles obtained from the adaptive observer scheme and the conventional MAF-PLL method when these parameters are suddenly changed at 0.5 s. It can be clearly seen that the estimated phase angle shows a good performance according to the measured one. In addition, the phase angle is still stable even when L_2 is varied instantly, which indicates that the proposed scheme can effectively stabilize the inverter system.

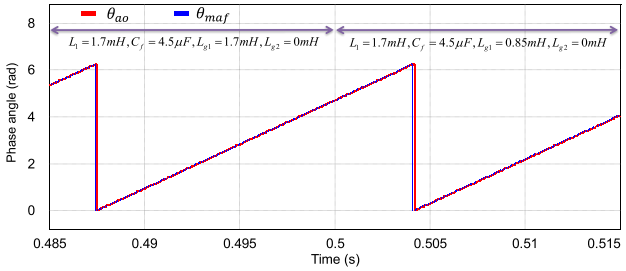

(a)

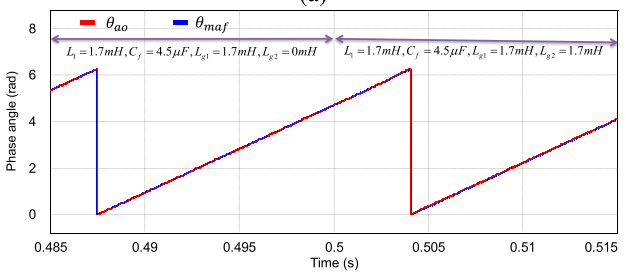

(b)

FIGURE 14. Simulation results for phase angle when L_2 is suddenly changed at 0.5 s. (a) L_{g1} decreases to 0.85*mH*. (b) L_{g2} increases to 1.7*mH*.

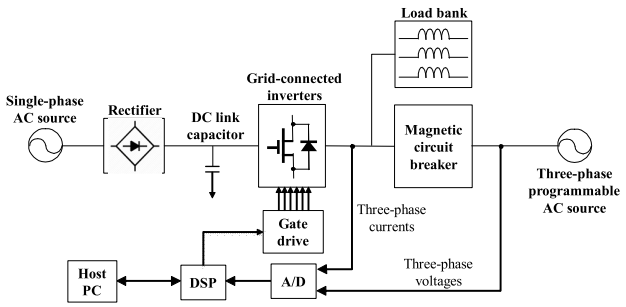

(a)

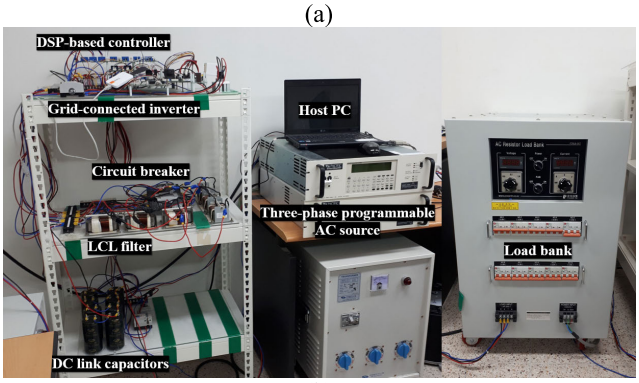

(b)

FIGURE 15. Experimental system. (a) Configuration of the experimental system. (b) Photograph of the experimental test set-up.

VI. EXPERIMENTAL RESULTS

To validate the feasibility of the proposed control scheme in a real system, the experimental results are also presented. Several test conditions such as the grid frequency variation, phase jump, and LCL parameter variations are considered to show the superiority of the proposed scheme. In addition, the experimental performance comparison is also given in this section. Fig. 15(a) shows the configuration of the experimental system to implement the proposed control scheme, which consists of a three-phase GCI with an LCL filter, a magnetic contactor for a grid connection, a DSP control board, and a three-phase programmable AC power source to generate distorted grid voltage and grid frequency variation. Fig. 15(b) shows the photograph of the experimental set-up. The entire control algorithm is implemented on a 32-bit floating-point DSP TM320F28335 with a sampling period of 100 μs to control 2 kVA prototype GCI [43]. Only the grid-side current sensors and grid voltage sensors are used for measurement to realize the proposed control algorithm.

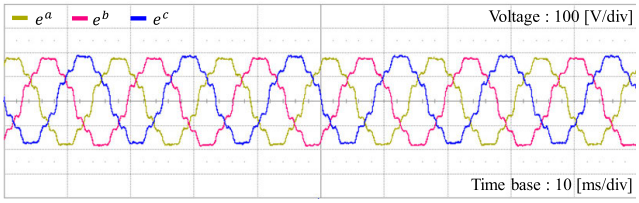

FIGURE 16. Three-phase distorted grid voltages produced by programmable AC source in experiments.

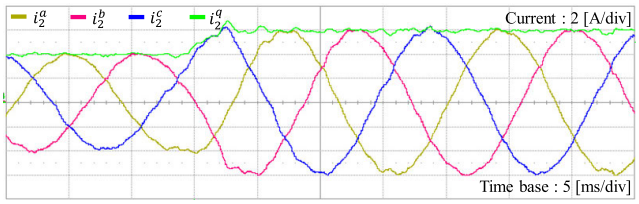

FIGURE 17. Experimental result for transient response of grid-side currents with the proposed scheme under step change in the current reference.

Fig. 16 shows three-phased distorted grid voltages which include the harmonics in the orders of 5^{th}, 7^{th}, 11^{th}, and 13^{th} with 5% magnitude of the fundamental component. These distorted grid voltages generated by the programmable AC power source are used in all the experiments to assess the performance of the proposed scheme.

Fig. 17 represents the experimental result for the transient response of grid-side currents with the proposed scheme under a step change in the current reference from 4 A to 6 A. The transient response shows that the grid-side currents rapidly track new reference within 5 ms. In addition, after transient periods, steady-state grid-side currents are fairly sinusoidal waveforms under the distorted grid voltage as in Fig. 16.

To ensure that the proposed control scheme retains a frequency-adaptive capability, the grid frequency is varied by a three-phase programmable AC power source. Fig. 18 shows the experimental results for the proposed control scheme under both distorted grid voltages and frequency variation. Fig. 18(a) shows the frequency estimation and three-phase grid-side current response when the grid frequency is suddenly changed from 60 Hz to 58 Hz. In order to achieve the frequency-adaptive capability in current control, the estimated frequency is obtained from the adaptive observer and is used to update the frequency information in the resonant

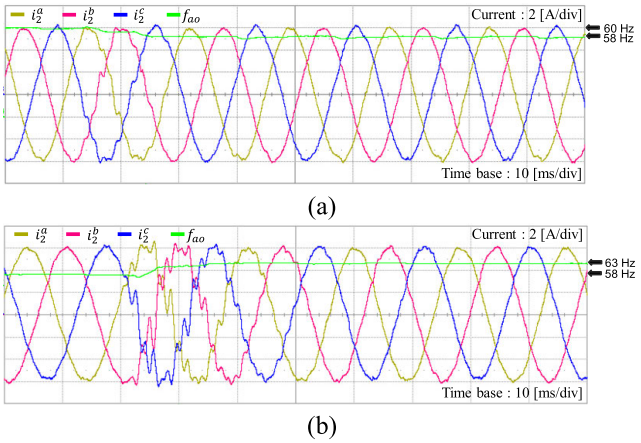

FIGURE 18. Experimental results for the proposed control scheme under distorted grid voltages and frequency change. (a) Three-phase grid-side currents and estimated frequency when the frequency is changed from 60 Hz to 58 Hz. (b) Three-phase grid-side currents and estimated frequency when the frequency is changed from 58 Hz to 63 Hz.

control terms. During transient periods before the estimated frequency converges to the actual value, the current waveforms show harmonic distortion. However, this harmonic distortion in currents is rapidly removed within one fundamental cycle as the grid frequency is precisely estimated. Fig. 18(b) shows the estimated frequency and three-phase grid-side current response when the grid frequency is instantaneously increased from 58 Hz to 63 Hz. The harmonic distortion in currents is slightly worse than the case of frequency drop because the frequency rise is higher (5 Hz). Even in this case, however, the proposed control scheme can recover sinusoidal current waveforms in about 1.5 cycles. The experimental results for both scenarios clearly demonstrate a fast transient and frequency-adaptive capability of the proposed control scheme.

To further evaluate the performance of the proposed control scheme, a comparison of transient response with several studies in [21], [44], and [45] is presented. In [21], the transient time under frequency variation is approximately 2 s for both the cases of frequency increase and decrease. This scheme also shows current overshoots even under ± 3 Hz frequency variation with a similar distorted grid during the transient period when the frequency varies. Even though another frequency-adaptive scheme based on IIR filter in [44] produces unnoticeable current overshoot when the frequency fluctuates from 50 Hz to 55 Hz, the controller takes approximately 3 cycles to reach the steady-state condition. The study in [45] shows current overshoot and long transient time of around 80 ms when the frequency drops from 60 Hz to 50 Hz. Also, the estimated frequency from the MAF-PLL shows undershoot before reaching the steady-state. On the other hand, the proposed control scheme shows barely noticeable peak current during the transient period and can manage to recover sinusoidal grid-side currents during 40 - 60 ms in the cases of frequency increase and decrease even in the presence of severely distorted voltages.

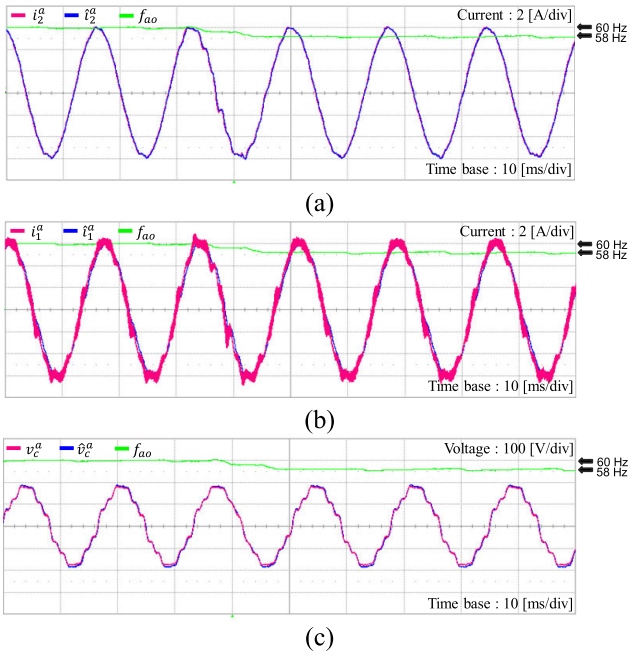

FIGURE 19. Experimental results for the estimation performance of discrete-time full-state observer under frequency change. (a) Measured and estimated state of grid-side currents. (b) Measured and estimated state of inverter-side currents. (c) Measured and estimated state of capacitor voltages.

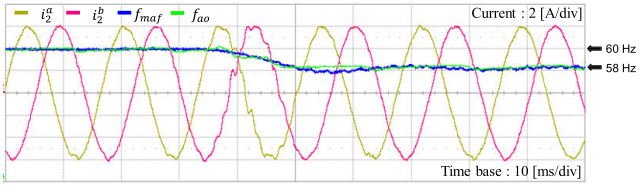

FIGURE 20. Experimental performance comparison for frequency estimation between the MAF-PLL and the adaptive observer.

Fig. 19 represents the experimental results for the estimation performance of the discrete-time observer under both distorted grid voltage and frequency variation. In these results, only the frequency decrease from 60 Hz to 58 Hz is considered. The estimated frequency is also shown together with the observer estimating performance in each figure. Fig. 19(a), Fig. 19(b), and Fig. 19(c) depict the measured and estimated states of the grid-side current, inverter-side current, and capacitor voltage for *a*-phase, respectively. It is shown that all the estimated states converge well to the measured values even under both distorted grid voltage and frequency variation.

Fig. 20 shows the performance comparison for frequency estimation in an experimental way between the conventional MAF-PLL and adaptive observer. It is clearly seen from the waveforms that the adaptive observer is faster than the MAF-PLL to estimate the grid frequency, which is well coincident with the simulation in Fig. 7. Moreover, the MAF-PLL method suffers from undershoot before reaching the steady-state condition.

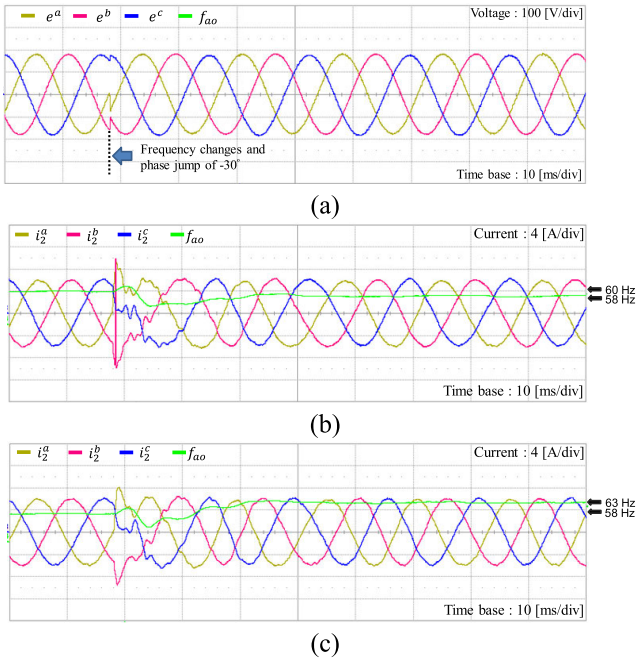

FIGURE 21. Experimental results for the proposed control scheme under both frequency change and phase jump of −30° with the ideal grid voltage. (a) Grid voltage. (b) Three-phase grid-side currents and estimated frequency under frequency change from 60 Hz to 58 Hz and phase jump of −30°. (c) Three-phase grid-side currents and estimated frequency under frequency change from 58 Hz to 63 Hz and phase jump of −30°.

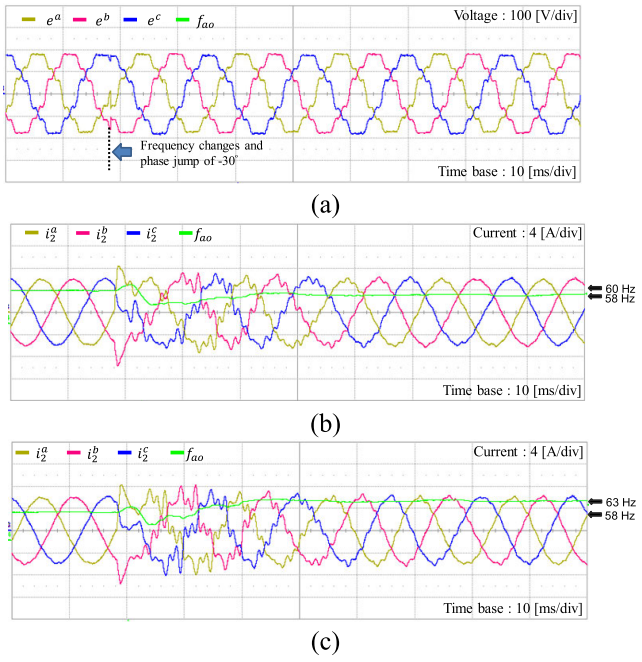

FIGURE 22. Experimental results for the proposed control scheme under both frequency change and phase jump with the distorted grid voltage. (a) Grid voltage. (b) Three-phase grid-side currents and estimated frequency under frequency change from 60 Hz to 58 Hz and phase jump −30°. (c) Three-phase grid-side currents and estimated frequency under frequency change from 58 Hz to 63 Hz and phase jump −30°.

To examine the performance of the proposed control scheme in another test environment, a phase jump is added beside the frequency variation. Fig. 21 shows the experimental results for the proposed control scheme under both the frequency change and phase jump of −30° with the ideal grid voltage. Fig. 21(a) represents the ideal grid voltages with frequency change and phase jump. Fig. 21(b) and Fig. 21(c) show the current response and estimated frequency under those two conditions mentioned. It can be seen that the frequency estimation takes a longer time to reach the final correct value and shows a slight undershoot due to a sudden phase jump.

Similarly, Fig. 22 represents the experimental results for the proposed control scheme when the grid voltages have frequency variation, phase jump of −30°, and harmonic distortion at the same time. Fig. 22(a) shows distorted grid voltages with frequency variation and phase jump, which are used for this test. As compared to Fig. 21(b) and Fig. 21(c), the transient response in Fig. 22(b) and Fig. 22(c) takes longer time to fully recover phase-current waveforms into sinusoidal after being applied the frequency change and phase jump. However, the grid-side current distortion caused by the frequency change and phase jump is completely removed approximately within three fundamental cycles for both the frequency increase and decrease conditions.

Fig. 23 shows the experimental results for the steady-state response of the grid-side currents under distorted grid voltages and frequency variation. Fig. 23(a) and Fig. 23(b) depict steady-state three-phase current waveforms and FFT result of a-phase grid-side current at 60 Hz. Similarly, Fig. 23(c) and Fig. 23(d) show the same results for 58 Hz. In FFT results shown in Fig. 23(b) and Fig. 23(d), the harmonic limits specified by the grid interconnection regulation IEEE Std. 1547 are also shown for each harmonic component. At steady-state, the current waveforms are quite sinusoidal and the current harmonic components are well damped by the proposed control scheme.

Hereinafter, to validate that the proposed control scheme is robust against the perturbation caused by LCL filter parameter variations, Fig. 24 represents the experimental test results for the proposed current controller when a different set of LCL filters are employed. Fig. 24(a) and Fig. 24(b) show steady-state and transient responses of three-phase grid-side currents. The transient current response immediately reaches the steady-state condition under the step change in current reference, and steady-state currents are sufficiently sinusoidal to meet the grid criteria. These results prove the robustness of the proposed control scheme against parameter uncertainties.

To test the robustness of the proposed control scheme under instantaneous parameter variation, a sudden change of L_2 value is applied during the operation of GCI. Fig. 25 shows the experimental result for the proposed control scheme when L_2 parameter is significantly increased to 3.3 times the nominal value. Even under such a large and sudden variation of L_2 parameter, only a slight current distortion is observed and phase-currents are recovered to sinusoidal waveform

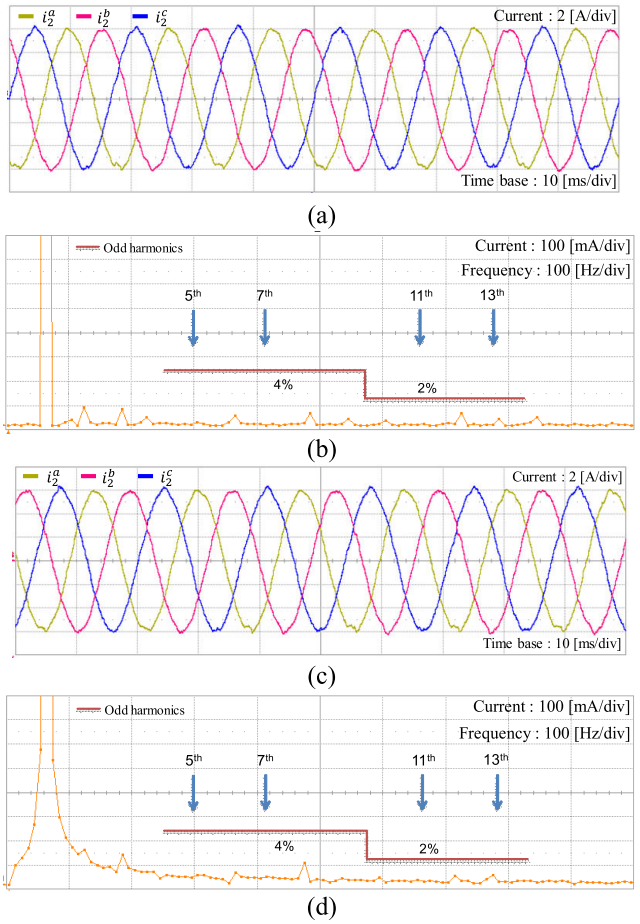

FIGURE 23. Experimental results for steady-state grid-side currents of the proposed control scheme under both distorted grid voltages and frequency change. (a) Steady-state grid-side current waveforms at 60 Hz. (b) FFT result for *a*-phase current at 60 Hz. (c) Steady-state grid-side current waveforms at 58 Hz. (d) FFT result for *a*-phase current at 58 Hz.

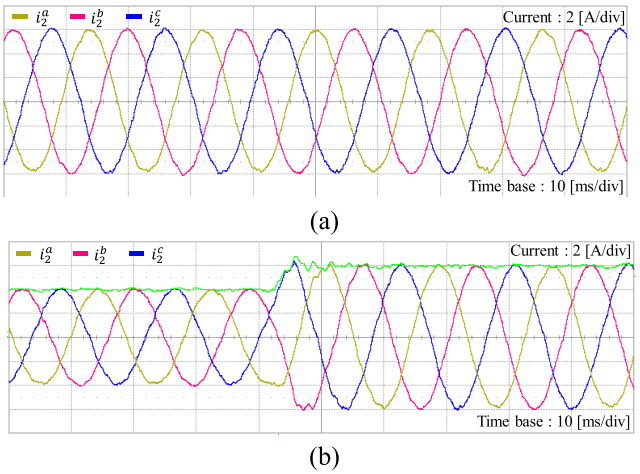

FIGURE 24. Experimental results for three-phase grid-side currents of the proposed control scheme under LCL filter parameter variation into $L_1 = 3.0mH$, $C_f = 6\mu F$, $L_2 = 1.0mH$. (a) Steady-state current response. (b) Transient currents response.

immediately in less than one fundamental cycle. This proves that the proposed control scheme has not only the robustness against parameter uncertainty but also fast transient response.

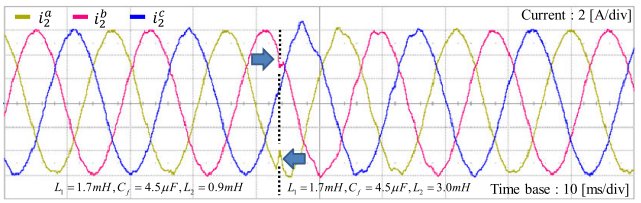

FIGURE 25. Experimental result for the proposed control scheme under sudden change of L_2 to 3.0 *mH*.

TABLE 2. Execution time of the proposed control scheme.

LMI-LQR-based current controller	8 µs
LMI-LQR-based full-state observer	10 µs
Adaptive observer	12 µs
Space vector modulation + data acquisition + etc.	40 µs
Full algorithm	70 µs

The execution time to implement the proposed robust frequency-adaptive current control scheme on the DSP is presented in Table 2 in detail. The total execution time to run the whole algorithm requires 70 μs. This is only 70% of the sampling period T_s, which is acceptable and can be implemented easily on the commercial DSP.

VII. CONCLUSION

In this paper, a robust frequency-adaptive current control of a GCI based on LMI-LQR under polytopic uncertainties in LCL filter parameters has been presented to ensure high-quality grid currents in the presence of grid voltage harmonic distortion, grid frequency variation, and polytopic uncertainties in the LCL filter parameters. The proposed control scheme is implemented in the SRF by augmenting integral and resonant terms into the LCL-filtered inverter system model to construct an integral-resonant full-state feedback control. An adaptive observer is also introduced for the grid frequency estimation which is used to adaptively adjust the frequency information in the resonant controller. Furthermore, in order to reduce the system cost and complexity caused by additional measurement, a discrete-time full-state observer is implemented in the stationary reference frame for the purpose of estimating the inverter states irrespective of operating grid frequency.

In general, the state-feedback control suffers from the difficulty in selecting feedback gain as the number of system states is increased. Moreover, the system model also has uncertainty due to parameter variation. In order to guarantee the robustness against LCL parameter uncertainty as well as to choose optimal gains for both the controller and observer systematically, an LMI-LQR-based design approach is applied in this paper. The effectiveness of the proposed current control scheme has been validated through the simulation and experiments under distorted grid voltage, frequency change, and LCL filter parameter variation. As a result, the proposed control scheme is able to overcome the issue related to parameter uncertainties while

maintaining frequency-adaptive control performance. It is confirmed through the simulation and experimental results that the proposed controller has the robustness against LCL filter perturbation even for instant change of parameters during inverter operation.

REFERENCES

[1] F. Blaabjerg, Y. Yang, D. Yang, and X. Wang, "Distributed power-generation systems and protection," *Proc. IEEE*, vol. 105, no. 7, pp. 1311–1331, Jul. 2017.

[2] Q.-N. Trinh and H.-H. Lee, "An advanced current control strategy for three-phase shunt active power filters," *IEEE Trans. Ind. Electron.*, vol. 60, no. 12, pp. 5400–5410, Dec. 2013.

[3] Y. Jia, J. Zhao, and X. Fu, "Direct grid current control of LCL-filtered grid-connected inverter mitigating grid voltage disturbance," *IEEE Trans. Power Electron.*, vol. 29, no. 3, pp. 1532–1541, Mar. 2014.

[4] W. Wu, Y. Sun, M. Huang, X. Wang, H. Wang, F. Blaabjerg, M. Liserre, and H. S.-H. Chung, "A robust passive damping method for LLCL-filter-based grid-tied inverters to minimize the effect of grid harmonic voltages," *IEEE Trans. Power Electron.*, vol. 29, no. 7, pp. 3279–3289, Jul. 2014.

[5] C. A. Busada, S. Gomez Jorge, and J. A. Solsona, "Full-state feedback equivalent controller for active damping in LCL-filtered grid-connected inverters using a reduced number of sensors," *IEEE Trans. Ind. Electron.*, vol. 62, no. 10, pp. 5993–6002, Oct. 2015.

[6] D. Pan, X. Ruan, and X. Wang, "Direct realization of digital differentiators in discrete domain for active damping of LCL-type grid-connected inverter," *IEEE Trans. Power Electron.*, vol. 33, no. 10, pp. 8461–8473, Oct. 2018.

[7] M. S. Sadabadi, A. Haddadi, H. Karimi, and A. Karimi, "A robust active damping control strategy for an LCL-based grid-connected DG unit," *IEEE Trans. Ind. Electron.*, vol. 64, no. 10, pp. 8055–8065, Oct. 2017.

[8] J. Xu, S. Xie, B. Zhang, and Q. Qian, "Robust grid current control with impedance-phase shaping for LCL-filtered inverters in weak and distorted grid," *IEEE Trans. Power Electron.*, vol. 33, no. 12, pp. 10240–10250, Dec. 2018.

[9] S. Silwal, S. Taghizadeh, M. Karimi-Ghartemani, M. J. Hossain, and M. Davari, "An enhanced control system for single-phase inverters interfaced with weak and distorted grids," *IEEE Trans. Power Electron.*, vol. 34, no. 12, pp. 12538–12551, Dec. 2019.

[10] A. Shayestehfard, S. Mekhilef, and H. Mokhlis, "IZDPWM-based feedforward controller for grid-connected inverters under unbalanced and distorted conditions," *IEEE Trans. Ind. Electron.*, vol. 64, no. 1, pp. 14–21, Jan. 2017.

[11] R. Guzman, L. G. De Vicuna, M. Castilla, J. Miret, and J. De La Hoz, "Variable structure control for three-phase LCL-filtered inverters using a reduced converter model," *IEEE Trans. Ind. Electron.*, vol. 65, no. 1, pp. 5–15, Jan. 2018.

[12] J. A. Rohten, J. R. Espinoza, J. A. Munoz, M. A. Perez, P. E. Melin, J. J. Silva, E. E. Espinosa, and M. E. Rivera, "Model predictive control for power converters in a distorted three-phase power supply," *IEEE Trans. Ind. Electron.*, vol. 63, no. 9, pp. 5838–5848, Sep. 2016.

[13] Q. N. Trinh, P. Wang, Y. Tang, and F. H. Choo, "Mitigation of DC and harmonic currents generated by voltage measurement errors and grid voltage distortions in transformerless grid-connected inverters," *IEEE Trans. Energy Convers.*, vol. 33, no. 2, pp. 801–813, Jun. 2018.

[14] M. Elkayam and A. Kuperman, "Optimized design of multiresonant AC current regulators for single-phase grid-connected photovoltaic inverters," *IEEE J. Photovolt.*, vol. 9, no. 6, pp. 1815–1818, Nov. 2019.

[15] Y. Yang, K. Zhou, and F. Blaabjerg, "Enhancing the frequency adaptability of periodic current controllers with a fixed sampling rate for grid-connected power converters," *IEEE Trans. Power Electron.*, vol. 31, no. 10, pp. 7273–7285, Oct. 2016.

[16] Q. Zhao, S. Chen, S. Wen, B. Qu, and Y. Ye, "A frequency adaptive PIMR-type repetitive control for a grid-tied inverter," *IEEE Access*, vol. 6, pp. 65418–65428, 2018.

[17] G. A. Ramos, R. A. Soto-Perez, and J. A. Cifuentes, "A varying frequency LPV-based control strategy for three-phase inverters," *IEEE Trans. Ind. Electron.*, vol. 64, no. 9, pp. 7599–7608, Sep. 2017.

[18] C. Wu, H. Nian, B. Pang, and P. Cheng, "Adaptive repetitive control of DFIG-DC system considering stator frequency variation," *IEEE Trans. Power Electron.*, vol. 34, no. 4, pp. 3302–3312, Apr. 2019.

[19] D. J. Hogan, F. J. Gonzalez-Espin, J. G. Hayes, G. Lightbody, and R. Foley, "An adaptive digital-control scheme for improved active power filtering under distorted grid conditions," *IEEE Trans. Ind. Electron.*, vol. 65, no. 2, pp. 988–999, Feb. 2018.

[20] R. Bimarta, T. V. Tran, and K.-H. Kim, "Frequency-adaptive current controller design based on LQR state feedback control for a grid-connected inverter under distorted grid," *Energies*, vol. 11, no. 10, p. 2674, Oct. 2018.

[21] F. Huerta, J. Perez, S. Cobreces, and M. Rizo, "Frequency-adaptive multiresonant LQG state-feedback current controller for LCL-filtered VSCs under distorted grid voltages," *IEEE Trans. Ind. Electron.*, vol. 65, no. 11, pp. 8433–8444, Nov. 2018.

[22] C. Zhang, X. Zhao, X. Wang, X. Chai, Z. Zhang, and X. Guo, "A grid synchronization PLL method based on mixed second- and third-order generalized integrator for DC offset elimination and frequency adaptability," *IEEE J. Emerg. Sel. Topics Power Electron.*, vol. 6, no. 3, pp. 1517–1526, Sep. 2018.

[23] Z. Dai, W. Lin, and H. Lin, "Estimation of single-phase grid voltage parameters with zero steady-state error," *IEEE Trans. Power Electron.*, vol. 31, no. 5, pp. 3867–3879, May 2016.

[24] I. Fitri, J.-S. Kim, and H. Song, "A robust suboptimal current control of an interlink converter for a hybrid AC/DC microgrid," *Energies*, vol. 11, no. 6, p. 1382, May 2018.

[25] L. A. Maccari, Jr., J. R. Massing, L. Schuch, C. Rech, H. Pinheiro, R. C. L. F. Oliveira, and V. F. Montagner, "LMI-based control for grid-connected converters with LCL filters under uncertain parameters," *IEEE Trans. Power Electron.*, vol. 29, no. 7, pp. 3776–3785, Jul. 2014.

[26] N.-B. Lai and K.-H. Kim, "Robust control scheme for three-phase grid-connected inverters with LCL-filter under unbalanced and distorted grid conditions," *IEEE Trans. Energy Convers.*, vol. 33, no. 2, pp. 506–515, Jun. 2018.

[27] J. S. Lim, C. Park, J. Han, and Y. I. Lee, "Robust tracking control of a three-phase DC-AC inverter for UPS applications," *IEEE Trans. Ind. Electron.*, vol. 61, no. 8, pp. 4142–4151, Aug. 2014.

[28] G. G. Koch, L. A. Maccari, Jr., R. C. L. F. Oliveira, and V. F. Montagner, "Robust H_∞ state feedback controllers based on LMIs applied to grid-Connected Converters," *IEEE Trans. Ind. Electron.*, vol. 66, no. 8, pp. 6021–6031 Aug. 2019.

[29] G. Willmann, D. F. Coutinho, L. F. A. Pereira, and F. B. Libano, "Multipleloop H_∞ control design for uninterruptible power supplies," *IEEE Trans. Ind. Electron.*, vol. 54, no. 3, pp. 1591–1602, Jun. 2007.

[30] S. J. Yoon, N. B. Lai, and K. H. Kim, "A systematic controller design for a grid-connected inverter with LCL filter using a discrete-time integral state feedback control and state observer," *Energies*, vol. 11, no. 2, p. 437, Feb. 2018.

[31] D. Brian, O. Andersen, and J. B. Moore, *Optimal Control: Linear Quadratic Methods*. London, U.K.: Prentice-Hall, 1989.

[32] J. J. E. Slotine and W. Li, *Applied Nonlinear Control*. Englewood Cliffs, NJ, USA: Prentice-Hall, 1991.

[33] T. V. Tran and K.-H. Kim, "Frequency adaptive grid voltage sensorless control of LCL-filtered inverter based on extended model observer," *IEEE Trans. Ind. Electron.*, to be published, doi: 10.1109/tie.2019.2944075.

[34] R. C. Dorf and R. H. Bishop, *Modern Control Systems*. Upper Saddle River, NJ, USA: Prentice-Hall, 2008.

[35] K. Ogata, *Modern Control Engineering*. Englewood Cliffs, NJ, USA: Prentice-Hall, 2010.

[36] S. Boyd, L. El Ghaoui, E. Feron, and V. Balakrishnan, *Linear Matrix Inequalities in System and Control Theory*. Philadelphia, PA, USA: SIAM, 1994.

[37] C. L. Phillips and H. T. Nagle, *Digital Control System Analysis and Design*. Englewood Cliffs, NJ, USA: Prentice-Hall, 1995.

[38] *IEEE Standard for Interconnecting Distributed Resources with Electric Power System*, IEEE Standard 1547, New York, NY, USA, 2003.

[39] S. Golestan, M. Ramezani, J. M. Guerrero, F. D. Freijedo, and M. Monfared, "Moving average filter based phase-locked loops: Performance analysis and design guidelines," *IEEE Trans. Power Electron.*, vol. 29, no. 6, pp. 2750–2763, Jun. 2014.

[40] X. Zhang, D. Xia, Z. Fu, G. Wang, and D. Xu, "An improved feedforward control method considering PLL dynamics to improve weak grid stability of grid-connected inverters," *IEEE Trans. Ind. Appl.*, vol. 54, no. 5, pp. 5143–5151, Sep. 2018.

[41] K. N. Narayanan, S. Shan, and L. Umamand, "Stability analysis of phase locked loop controllers for grid tied inverters in weak microgrids," in *Proc. PEDES*, Chennai, India, Jun. 2014, vol. 29, no. 6, pp. 2750–2763.

[42] M. Said-Romdhane, M. Naouar, I. Belkhodja, and E. Monmasson, "An improved LCL filter design in order to ensure stability without damping and despite large grid impedance variations," *Energies*, vol. 10, no. 3, p. 336, Mar. 2017.
[43] *TMS320F28335 Digital Signal Controller (DSC)—Data Manual*, Texas Instrum., Dallas, TX, USA, 2008.
[44] F. Gonzalez-Espin, I. Patrao, E. Figueres, and G. Garcera, "An adaptive digital control technique for improved performance of grid connected inverters," *IEEE Trans. Ind. Informat.*, vol. 9, no. 2, pp. 708–718, May 2013.
[45] S.-J. Yoon and K.-H. Kim, "Multiloop current control for an inductive–capacitive–inductive-filtered grid-connected inverter with frequency-adaptive capability under distorted grid environment," *IET Power Electron.*, vol. 12, no. 6, pp. 1521–1531, May 2019.

RIZKA BIMARTA was born in Yogyakarta, Indonesia, in 1991. She received the B.S. degree from Gadjah Mada University, Yogyakarta, in 2014. She is currently pursuing the M.S. degree with the Department of Electrical and Information Engineering, Seoul National University of Science and Technology. She worked at Samsung Electronics Indonesia as a Product Engineer. Her research interests include robust control, renewable energy, and power electronics.

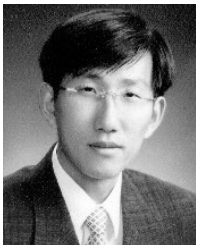

KYEONG-HWA KIM (Member, IEEE) was born in Seoul, South Korea, in 1969. He received the B.S. degree in electrical engineering from Hanyang University, Seoul, in 1991, and the M.S. and Ph.D. degrees in electrical engineering from the Korea Advanced Institute of Science and Technology (KAIST), Daejeon, South Korea, in 1993 and 1998, respectively. From 1998 to 2000, he was a Research Engineer with Samsung Electronics Company, South Korea, where he was involved in the research and development of AC machine drive systems. From 2000 to 2002, he was a Research Professor with KAIST. From August 2010 to August 2011, he was a Visiting Scholar with the Virginia Polytechnic Institute and State University (Virginia Tech), Blacksburg, VA, USA. Since August 2002, he has been with the Seoul National University of Science and Technology, Seoul, where he is currently a Professor. His current research interests include AC machine drives, the control and diagnosis of power systems, power electronics, renewable energy, and DSP-based control applications. Prof. Kim is a member of the Korean Institute of Power Electronics (KIPE).